Universidade de São Paulo

Instituto de Astronomia, Geofísica e Ciências
Atmosféricas Departamento de Geofísica

Kleber Joshua Sanmartin

Geomagnetic paleosecular variation for the past 1Ma recorded in lava flows from south Ecuador

São Paulo
2022

KLEBER JOSHUA SANMARTIN

Geomagnetic paleosecular variation for the past 1Ma recorded in lava flows from south Ecuador

Versão Original

<div style="margin-left:50%">

Dissertação apresentada ao Departamento de GeofÍsica do Instituto de Astronomia, Geofísica e Ciências Atmosféricas da Universidade de São Paulo como requisito parcial para obtenção do título de Mestre em Ciências.

Área de concentração: Geofísica.

Orientador: Prof. Dr. Ricardo Ivan Ferreira da Trindade.

</div>

São Paulo
2022

To my family, my tutor, and friends, especially to my parents Kleber and Marcia.

Autorizo a reprodução e divulgação total ou parcial deste trabalho, por qualquer meio convencional ou eletrônico, para fins de estudo e pesquisa, desde que citada a fonte.

RESUMO

Estudos de variação paleosecular com boa cobertura geográfica e temporal são cruciais para entender o comportamento do campo magnético da Terra no passado. No hemisfério sul, mais especialmente no sul do Equador, esses dados são escassos. Registros confiáveis que podem ser obtidos de fluxos de lava são necessários para criar modelos de campo magnético mais precisos, especialmente para o hemisfério sul. Um total de 196 amostras de 23 fluxos de lava previamente datados de 9 vulcões diferentes foram submetidos a estudos magnéticos e paleodirecionais detalhados. A análise termomagnética mostra que o principal portador de magnetização é titanomagnetita pobre em Ti. Os parâmetros de histerese e as curvas de reversão de primeira ordem (FORCs) indicam que o tamanho do grão magnético varia de SD a PSD e as curvas de IRM revelam a predominância de minerais de baixa a média coercitividade. Desmagnetização térmica e de campos alternados foram usadas para obter direções de 23 sítios. A direção paleomagnetica média para o conjunto de sítios é $D = 355,4°$, $I = -1,1°$ (A95=7,6°). Trabalhos anteriores no Equador (Kent et al., 2010; Opdyke et al., 2006) são consistentes com essas direções. A direção média do paleopólo para todas as amostras é Plat= 85,4° N e Plon=199,6 E° (A95=7,6). Duas direções anômalas em relação ao GAD (Dipolo Geocêntrico Axial) coincidem com duas excursões magnéticas. O fluxo de lava SE03 (492 ± 9) está dentro do erro da excursão Orphan Knoll (~ 495 ka) identficada anteriormente em fluxos de lava nas Ilhas Galápagos (Equador). Além disso, a amostra SE21 (30 ± 3 ka) está dentro do intervalo da excursão Mono Lake. Uma comparação entre os movimentos morfotectônicos da falha de Pallatanga e um VGP inconsistente do vulcão Igualatá (SE14: 376 ± 10ka) reflete uma alta atividade tectônica nesta zona. Após aplicação do corte de Vandamme (1994), os nossos dados revelam uma dispersão (Sb) de 15.6° (Su = 19.10°; Sl = 11.56°). Este novo resultado é bastante semelhante ao Sb relatado anteriormente para a região com base em um conjunto menor de dados, e é 1.6° superior àqueles previstos pelos modelos G e TK03. Além da forte atividade tectônica, a distribuição de VGP é maior no Equador continental devido a uma forte variabilidade longitudinal associada a importantes componentes não dipolares que podem refletir os efeitos da Anomalia Magnética do Atlântico Sul.

Palavras-chave: Variação paleosecular, pólo geomagnético virtual, Arco vulcânico do Equador, Excursão magnética.

ABSTRACT

High-quality paleosecular variation studies with good geographical and temporal coverage are crucial for understanding the past Earth's magnetic field behavior. In the southern hemisphere, but especially in southern Ecuador, these data are still scarce. Reliable records that can be obtained from volcanic rocks, specifically from lava flows, are required to create more accurate magnetic field models especially for the southern hemisphere. A total of 196 samples from 23 previously dated lava flows from nine different volcanoes were subjected to detailed rock magnetic and paleodirectional study. Thermomagnetic analysis on the lava flows shows that the main carrier of magnetization is titanomagnetite with variable, but typically low level of Ti substitution. Hysteresis parameters and First Order Reversal Curves (FORCs) indicate that the magnetic grain size varies from SD to PSD and IRM curves reveals the predominance of low- to medium coercivity minerals. Stepwise thermal and alternating field demagnetization were used to obtain 23 site-mean directions. The mean direction from all sites is $D = 355.4°$, $I = -1.1°$ ($A95=7.6°$). These paleomagnetic directions are consistent with past works on Ecuador. The mean paleopole direction for all samples is Plat= 85.4° N, Plon=199.6 E° ($A_{95}=7.6$). Furthermore, two anomalous directions with respect to the GAD (Geocentrical Axial Dipole) coincide with two magnetic excursions. Lava flow SE03 (492 ± 9) lies within error as the Orphan Knoll excursion at ~495 ka, previously reported in lavas from Galápagos Island (Ecuador). Furthermore, sample SE21 (30 ±3 ka) falls within the range of the Mono Lake excursion. A comparison between morphotectonic movements from Pallatanga fault and an inconsistent VGP from Igualatá volcano (SE14: 376 ±10ka) reflects the high tectonic activity at this zone. After applying a Vandamme (1994) cutoff, our results show a dispersion (Sb) of 15.6° (Su = 19.10°; Sl = 11.56°). This new result is similar with the Sb reported previously for the region with a smaller amount of sites and is 1.6° higher than those predicted by G and TK03 models. Besides the strong tectonic activity, VGP distribution is higher at continental Ecuador due to a strong longitudinal variability associated with important non-dipolar components of the field, which can be associated to the South Atlantic Magnetic Anomaly.

Keywords: Paleosecular variation, Virtual Geomagnetic pole, Ecuadorian volcanic arc, Magnetic excursion.

TABLE OF CONTENTS

TABLE OF FIGURES

INTRODUCTION

1. INTRODUCTION

1.1. Background

The geocentric axial dipole (GAD) assumption, that states that through time the average geomagnetic field is that close to a GAD, is the basis for paleo and archeomagnetism. (Fisher, 1953; Hospers, 1954; McElhinny & McFadden, 1997; McElhinny & Merrill, 1975; Opdyke & Henry, 1969; Veikkolainen et al., 2014). (Hospers, 1954) introduced this term by the first time. However, in the !970's (e.g., Barbetti & Flude, 1979; Wilson, 1970) some studies have already shown departures of the GAD approximation on different time intervals primarily because of the presence of significant contributions of quadrupolar and octupolar axial components (see also Bloxham, 2000; Cromwell et al., 2018; C. L. Johnson et al., 2008).

The main magnetic field is generated at the outer core and shows fluctuations through the whole history of the Earth (Johnson & McFadden, 2015). Paleosecular variation studies are focused on the true temporal fluctuations in the Earth's magnetic field, discarding reversals, excursions and true polar wandering (e.g. Kent & Tauxe, 2005; Quidelleur & Courtillot, 1996; Roperch et al., 2015; Tauxe & Kent, 2004; Tauxe & Kodama, 2009). These studies usually comprise at least 5 million years intervals and are usually used for describing field variations during periods of unchanged polarity (Johnson & McFadden, 2015). Much of the plate reconstructions have been built thanks to the relationship between the forecasted latitude by the GAD model vs the inclination of the geomagnetic field, however the data obtained usually shows small disturbances due to other axial components. Consequently, paleomagnetism also seeks to achieve transformations of these vectors into virtual geomagnetic poles (VGP) and dipole moments (McElhinny & McFadden, 1997; Tauxe & Kodama, 2009).

Paleomagnetic results from high latitudes have greater angular dispersion of Virtual Geomagnetic Pole (VGP) compared with Equatorial paleomagnetic results (Mcfadden et al., 1988). Furthermore, this dispersion will be lower in periods of low frequency of geomagnetic reversals than in high frequency reversals (e.g., Biggin et al., 2008; Mcfadden et al., 1991). Specifically, for the purpose of the present work we will focus on the Matuyama–Brunhes (M–B) geomagnetic reversal (last polarity reversal, 786 ka) (Channell et al., 2010; Harrison, 1974; Hartl & Tauxe, 1996) on low-latitude sites of

Southern Ecuador. During this period, Balbas et al. (2018) and Singer et al. (2019) show that a field decay could start 30 ka before of M-B event. Brunhes and Matuyama chrons show different geomagnetic field geometries. For example, Brunhes has fewer reversals with a strong GAD predominance, while Matuyama shows a significant axial octupole contribution, but also a stronger latitudinal dependence of dispersion on each hemisphere (Northern = primordially negative inclination anomalies; and Southern = zero or positive inclination anomalies) (Johnson et al., 2008; Tauxe & Kent, 2004). Through the use of spherical harmonic equations for calculating the axial components for Brunhes and Matuyama the following values were obtained: (1) for Matuyama the values for axial quadrupole, and axial octupole as a percentage of axial dipole are 4.6%, and 2.1% respectively; and (2) for Brunhes the values for axial quadrupole, and axial octupole as a percentage of axial dipole are 2.6%, and 2.9% respectively (Johnson & McFadden, 2015).

The present research will focus on high-quality geographically widespread paleomagnetic results from the southern termination of the Ecuadorian volcanic arc (23 sites). We collected from lava flows from 8 volcanoes: Huisla, Mulmul, Igualata, Carihuairazo, Chimborazo, Sagoatoa, Licto cone, and Calpi cone. The purpose of this research will be: (1) test the reliability of the relationship of numerous volcanic edifices at this part of Ecuador, which are supposedly concomitant or influencing each other; (2) improve the scarce magnetic record in southern Ecuador, but also in continental Ecuador as a whole; (3) use the detailed data obtained to quantify the impact of the PSV indices on Ecuador (specially the axial components); (4) compare the data obtained with global paleosecular variations models.

1.2. Statement of the problem (Project Justification).

This project aims to better understand how the paleomagnetic field has been changing on equatorial latitudes. The more specific objectives are:

- Present new rock-magnetic and paleomagnetic results of well-dated material belonging to past volcanic eruptions in southern Ecuadorian Andes, which allow us to improve the global paleomagnetic database and the current geomagnetic models with new and modern laboratory techniques.

- Help fill the gap of paleomagnetic data in the southern hemisphere, near equatorial latitudes. Currently two-thirds of all data are from the Northern Hemisphere.

GEOLOGICAL SETTING

2. GEOLOGICAL SETTING

In Ecuador, the Nazca oceanic plate plunges beneath the South American continental plate, generating the Ecuadorian volcanic arc (Figure 1b). The Carnegie Range and the Grijalva Fracture Zone (GFZ) are the main features of the Nazca Plate, which started its subduction between 2 to 9 Ma (Gutscher et al., 1999; Witt et al., 2006). According to Hey, (1977) the Carnegie ridge started its creation by its motion over the Galapagos hotspot. This subduction lead the creation of the Ecuadorian volcanism (Hall & Wood, 1985) and two mountain ranges, the Western Cordillera (WC) and Eastern Cordillera (EC) forming the Ecuadorian Andes, divided by the Ecuadorian Inter-Andean valley (IAV) (Figure 1b) (Hall et al., 2008; Spikings et al., 2001). Volcanoes belonging to the Western Cordillera are mainly dacitic to andesitic in their composition (Samaniego et al., 1998). Conversely, volcanoes belonging to EC and the IAV are mainly andesitic in their composition (Hall & Mothes, 2008; Samaniego et al., 1998).

The eight studied volcanoes (Huisla, Mulmul, Igualata, Carihuairazo, Chimborazo, Sagoatoa, and Licto and Calpi cones) are part of the Ecuadorian Andes (Figure 1). These volcanoes were active at the Plio-Quaternary (Bablon et al., 2019; Barberi et al., 1988; M. L. Hall et al., 2008; M. L. Hall & Beate, 1991; M. L. Hall & Wood, 1985). The distribution of the volcanoes from Western Coordillera to Eastern Cordillera is Chimborazo (6268 m.a.s.l), Carihuairazo (5018 m.a.s.l), Calpi cone, Sagoatoa (4169 m.a.s.l), Puñalica (3988 m.a.s.l), Igualata (4430 m.a.s.l), Licto cone, Huisla (3763 m.a.s.l), Mulmul (3878 m.a.s.l) (Figure 1c).

The oldest edifice is the Sagoatoa volcano (> 800 ka) with an age of 1.73 ± 0.35 Ma, although there are some controversy about its age (see Lavenu et al., 1992 and Bablon et al., 2018). Subsequently, the activity from the Huisla volcano started (612 ka to 492 ka). Huisla volcano has been built by multiple plinian eruptions (Ordóñez, 2012). Pre-Carihuairazo and Carihuaraizo dating shows eruption contemporaneous to that of Huisla, with ages of 512 ka and 225 ka respectively (Bablon et al., 2019; Samaniego et al., 2012). Due to its morphology and erosion, Igualata volcano seems to be older than the previous volcanoes, but the oldest sample obtained from this volcano is dated at 376 ± 10 ka. Therefore, the contrasting erosion processes have taken place due to tectonic activity (Bablon et al., 2019) with the Pallatanga fault playing an important role on this process (Baize et al., 2020). Calpi and Licto scoria cones are located in the southeast area of the

study. A Lava flow from Licto cone is dated at 183 ± 9 ka. Bablon et al. (2019) suggest that Calpi cone formed in two stages between 62 ± 4 ka and 8 ± 5 ka. Finally, the Puñalica volcano is the youngest volcano (18 ± 3 ka) localized at the northeast of Carihuairazo (Bablon et al., 2018). Clapperton, (1990) suggest that Puñalica is part of Carihuairazo, which stopped its volcanic activity due to the extrusion of Puñalica volcano.

Bablon et al. (2019) used geochemical analyses to show a predominance of medium-K calc-alkaline rocks. Compositionally, the lava flows are predominantly basaltic andesites (e.g. Licto cone, one lava from Calpi cone, Puñalica volcano) to andesites (e.g. two lavas form Calpi cone) (Bablon et al., 2019). However, one lava flow at the top of Sagoatoa and one youngest lava flow from Huisla show a dacitic composition (Bablon et al., 2019).

Geochemistry data from Bablon et al. (2018) indicate that those volcanoes show the same composition pattern of other arc magmas, showing an enrichment of elements such as La, Ce, Nd in the first group and Rb, Ba, and K in the second group, comprising Large-Ion Lithophile Elements and Light Rare Earth Elements, respectively. In addition, it shows a retrenchment of Y, Nb, and Ta (High-Field Strength Elements).
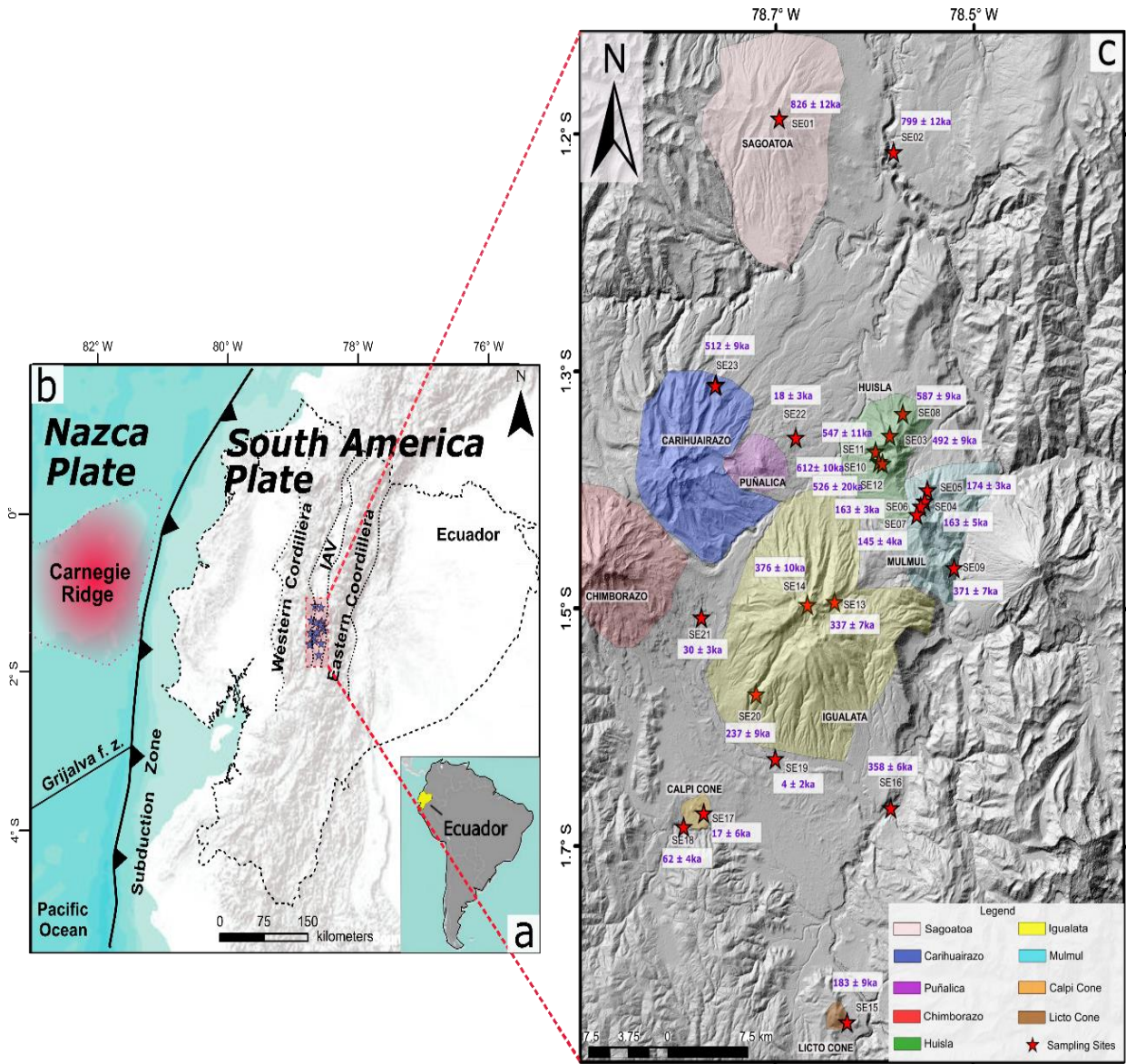
Figure 1. Geology and sampling site location. a) South America with Ecuador in yellow.
b) Geodynamic framework with study zone in a red rectangle; IAV Inter-Andean Valley.
c) Study area with different volcanoes and sampling sites (red stars) with ages.

PHYSICAL BASIS OF ROCK MAGNETISM AND PALEOMAGNETISM

3. PHYSICAL BASIS OF ROCK MAGNETISM AND PALEOMAGNETISM

This chapter will present some geophysical concepts and theories related with Rock magnetism and Paleomagnetism. The reference sources in this chapter are mainly Butler (1992), Halliday et al. (1972), McElhinny & McFadden (1999) and Tauxe et al. (2010).

3.1. Geomagnetic Field and Geomagnetic Parameters

The geometry of the GAD model (figure 2) means that the geomagnetic field is predominantly a dipolar field with an axis parallel to the Earth's rotation axis at least for the last 10 Ma. To be specific, it is like a simple magnetic dipole, positioned at the center of the Earth and aligned with its rotation axis (figure 2). Taking in account this assumption, we could correlate the latitude λ with the Inclination (I) by:

$$\tan I = 2 \tan \lambda \tag{1}$$

This equation is essential in paleomagnetism, being an immediate consequence of the GAD assumption for the geomagnetic field.
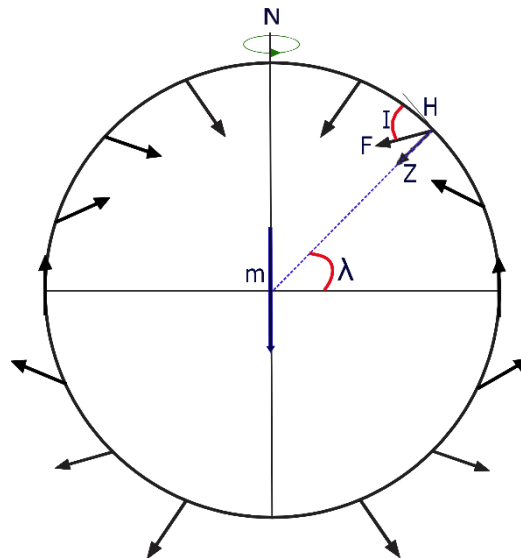
Figure 2. Direction of the Earth's field at the surface following a GAD assumption. The magnetic dipole m is placed in the center of the Earth, aligned with the axis of rotation; λ is the geographic latitude; r is the radius; I is Inclination; and N is the geographic north. Taken and modified from Butler (1992) and references therein.

It is possible to calculate the magnetic field orientation and strength. For a given latitude, the equations for calculate the vertical (Z) and horizontal (H) components are:

$$H = \left(\frac{\mu_0 * m * \cos \lambda}{4\pi r^2}\right), \tag{2}$$

$$Z = \left(\frac{2\mu_0 * m * \sin \lambda}{4\pi r^2}\right), \tag{3}$$

being m the magnetic moment, r the Earth´s radius and µ is the magnetic permeability of the substance between the poles ($\mu_{\circ} = 1$ in the vacuum). In addition, the field strength (F) is given by:

$$F = (X^2 + Y^2 + Z^2)^{\frac{1}{2}} = (H^2 + Z^2)^{\frac{1}{2}}, \tag{4}$$

replacing the equations (2) and (3) in (4), the field strength is then given by:

$$F = \frac{\mu_{\circ} m}{4\pi r^2}(1 + 3\sin^2 \lambda)^{\frac{1}{2}} \tag{5}$$

Earth´s magnetic field at any coordinate is generally described in terms of magnitude ($\vec{B}$), declination (D) and inclination (I) (Figure 3a). For example, Z is pointed downwards, X is pointed to the geographic north, Y is pointed to the geographic east, D is the angle between the horizontal component and the geographic north, and I is the angle between the field vector with respect to the horizontal plane (Figure 3a). The line where $I = 0°$ forms the magnetic equator, while the two points where $I = 90°$ and $I = −90°$ are the so-called "real magnetic poles" (figure 3b).
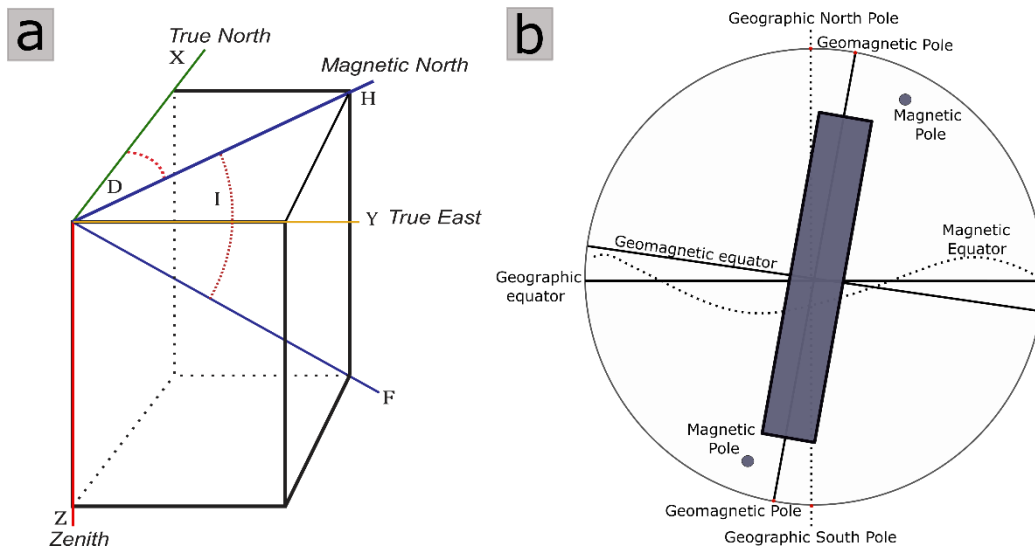
Figure 3. a) Components of Earth's Magnetic Field; b) Comparison between Geographic, Geomagnetic and Magnetic Poles. (modified from Mcelhinny, 1973).

The force of interaction between two poles is given by the equation

$$F = \mu \left(\frac{m1 * m2}{r^2}\right), \tag{6}$$

where m1 and m2 are the pole strength, r is the distance that separates them and μ is the magnetic permeability of the substance between the poles ($\mu_\circ = 1$ in the vacuum). Furthermore, for the vacuum case the magnetic field $\vec{H}$, and the magnetic flux density (magnetic induction) $\vec{B}$ are related by the equation

$$B = \mu_\circ H, \tag{7}$$

Another important parameter is the magnetization ($\vec{J}$). It is defined as the sum of the magnetic moments ($\vec{M}$) of a material per unit volume (V) :

$$J = M/V, \tag{8}$$

where $\vec{M}$ is described as:

$$\vec{M} = \lim_{\triangle V \to 0} \sum_{r=0}^{n} \frac{m_r}{\triangle V} \tag{9}$$

Finally, the relationship between $\vec{B}, \vec{H},$ and $\vec{M}$ is given by:

$$B = \mu_\circ (J + H) \tag{10}$$

It is essential to observe that the magnetic induction $\vec{B}$ depends on the medium. On the other hand, the magnetic field $\vec{H}$ only depends on the charges and is independent of the medium.

Magnitude and direction from the magnetic field $\vec{H}$ is continuous, changing from normal to reverse polarity (Figure 4). Usually, more continuous changes occurring at a scale of centuries to millennia are named as secular variations, longer and more significant changes are related to excursions and polarity reversals. A normal polarity is when the north magnetic pole is coinciding roughly with the north geographic Pole, while the inverse configuration is named as reverse polarity (Figure 4). The current palaeomagnetic chron is characterized by normal polarity regime (Brunhes Chron).
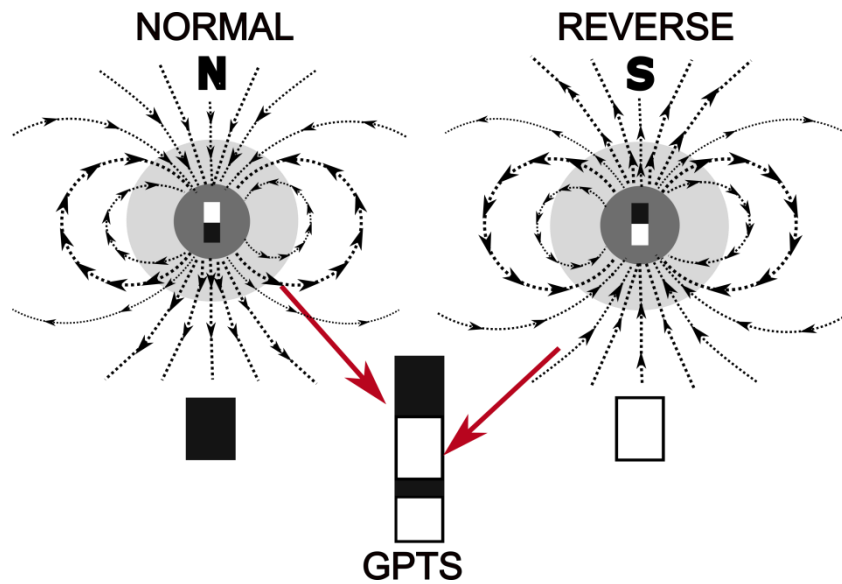
Figure 4. Representation of the Earth's magnetic field showing Normal (black square) and Reverse (white square) polarities and following a GAD assumption. Geomagnetic Polarity Time Scale (GPTS) normal polarity (black intervals) and reversed polarity (white intervals). Modified from Langereis et al. (2010).

3.2. Rock magnetic properties

This section will concern the main properties of magnetic minerals (Table 1), comprising ferrimagnetic and antiferrimagnetic minerals commonly used in paleomagnetism. Properties like susceptibility, Curie temperature, saturation and coercivity will be explained in order to provide the basic knowledge to understand the acquisition of the paleomagnetic records.

3.2.1. Magnetic susceptibility and its temperature variation

The magnetic susceptibility of a material can be seen as its ability to be magnetized when a magnetic field H is applied. In other words, it is defined as the ratio between the induced magnetization (M) and the intensity of the magnetic field (H) (Halliday et al., 1972).

$$\chi = \frac{M}{H},$$
(11)

where χ is the magnetic susceptibility, which is dimensionless.

In lava flows, magnetic minerals control the susceptibility. Based upon the magnetic properties of the minerals, the magnetic materials can be classified into diamagnetic, paramagnetic and ferromagnetic.

The anisotropy of magnetic susceptibility (AMS) is a physical property, which depicts the preferred orientation of the anisotropic magnetic minerals, known as magnetic fabric (Bouchez, 1997). AMS for each site can be geometrically understood as an ellipsoid of orthogonal axes. Where k1 > k2 > k3, being these, the three principal susceptibilities directions (maximum, intermediate and minimum, respectively) (Collinson, 1983). Usually in lava flows, the rocks are anisotropic with different susceptibility values for each orthogonal axes. The anisotropy of magnetic susceptibility is given by the following equations, and described as a second-order symmetric tensor,, where $k_{12} = k_{21}$, $k_{13} = k_{31}$, and $k_{23} = k_{32}$:

$$M_1 = k_{11}H_1 + k_{12}H_2 + k_{13}H_3 \qquad (12)$$

$$M_2 = k_{21}H_1 + k_{22}H_2 + k_{23}H_3 \qquad (13)$$

$$M_3 = k_{31}H_1 + k_{32}H_2 + k_{33}H_3 \qquad (14)$$

The direction with the highest magnetic susceptibility, or the magnetic lineation, corresponds to the axis k1, whereas the direction with the lowest magnetic susceptibility corresponds to the pole of the magnetic foliation and is denotes by k3. In lava flows, when the magnetic fabric is normal, the intermediate and maximum susceptibility axes (k2 and k1, respectively) must be distributed close to the horizontal plane, and the pole of the magnetic foliation k3 must be close to the vertical orientation (Bouchez, 1997). The mean of the three principal susceptibility directions corresponds to the mean magnetic susceptibility (Km).

$$K_m = \frac{k_1 + k_2 + k_3}{3} \qquad (15)$$

The shape of the anisotropy tensor is provided by the T-shape parameter, which varies from –1 (prolate ellipsoid, k1 >> k2 and k3) to +1 (oblate ellipsoid, k1 and k2 >> k3). Jelínek, (1981), calculate the T-shape parameter as:

$$T = 2ln(K2/K3)/ln(K1/K3) - 1, \qquad (16)$$

when T < 0 is prolate, T > 0 is oblate and T = 0 is a triaxial ellipsoid.

Nagata, (1961) calculates the degree of anisotropy through the following equation:

$$P = K1/K3 \qquad (17)$$

The sample is isotropic when P = 1, and P increases as the anisotropy of the rock increases. In addition to the degree of anisotropy, the magnetic lineation L = $k1/k2$ and magnetic foliation F = $k2/k3$ are also often used to denote the shape of the ellipsoid (Tarling and Hrouda, 1993).

3.2.2. Hysteresis

In Ferromagnetic materials, a region with uniform magnetization is known as magnetic domain. Regions that separate adjacent parts of a grain with different directions of spontaneous magnetization are known as domain walls. Hysteresis parameters provide data to analyse the structure of magnetic domains and therefore the stability of their remanence. It can also provide information about the occurrence of changes in magnetic mineralogy (chemical-mineralogical changes) and domain structure (physical changes).

Following a typical hysteresis cycle (figure 5), starting from very high magnetic fields, the magnetization of ferrimagnetic and antiferromagnetic minerals reaches saturation (Ms). At this point, all magnetic domains are oriented parallel to an external field (positive direction). When the magnetic field is reduced to zero, the material retains a part of the residual magnetization, which is called the remanent magnetization (Mrs). Lastly, the remaining coercive force (Hc) is the reverse magnetic field (negative diection) required to reduce the net magnetization of the material to zero from the value of remanence.
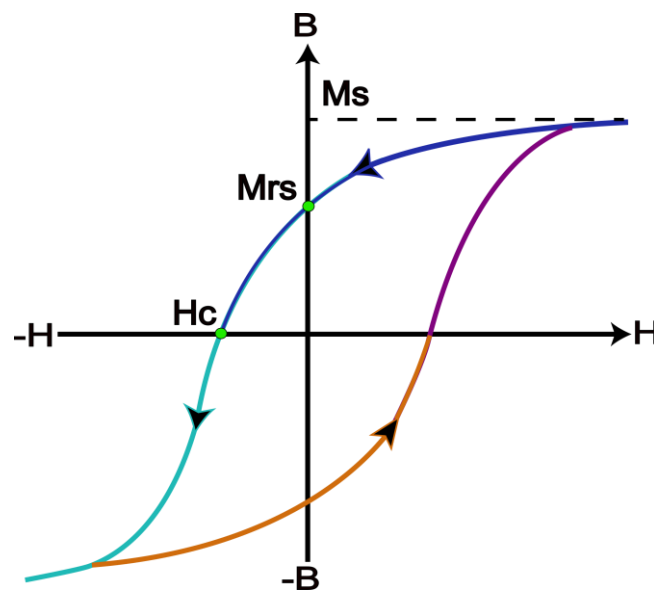
Figure 5. Hysteresis loops. Where H: applied magnetic field; B: induced magnetization; Ms: saturation magnetization; Mrs: remanent saturation magnetization; Hc: coercivity; Hcr: coercivity of remanence.

Table 1 Summarizes the principal magnetic properties of the main magnetic minerals used in paleomagnetism. Taken from Hunt et al. (1995).

Mineral	Chemical composition	Magnetic structure	Curie Temperature $(C°)$	Saturation Magnetization (Am^2/kg)	Coercivity (Hc)
Oxides					
Hematita Maghemita Ilmenita	$\alpha - Fe_2O_3$ $\gamma - Fe_2O_3$ $FeTiO_3$	Antiferromagnetic Ferrimagnetic Antiferromagneic	675 600 -233	.4 70-80 0	1.5-5 .3 -
Magnetita	Fe_2O_3	Ferrimagnetic	575-585	90-92	0,3
Sulfurs					
Pirrotita	Fe_7S_8	Ferrimagnetic	320	20	.5-1
Oxide-Hydroxide					
Goetita	$\alpha - FeOOH$	Antiferromagnetic	120	< 1	> 5

3.2.3. First Order Reversal Curves (FORC)

First order reversal curves (FORC) are partial hysteresis curves. A difference between FORC's and hysteresis curves is that hysteresis curves only show volumetric magnetic properties (Roberts et al., 2000). On the other hand, FORC are helpful to better understand the mineral components of the samples, their domain structures, switching field distributions, and reversal mechanisms (Pike et al., 1999, 2001; Roberts et al., 2000).

The first step to develop a FORC diagram is to saturate the sample by applying a high positive magnetic field. Secondly, the magnetic field is decreased to an opposite value (Hr). The magnetic field is increased again until reaching saturation, but this time passing through a point (Hb) (Figure 6). This process is repeated multiple times until a FORC diagram is obtained (Pike et al., 1999; Roberts et al., 2000).
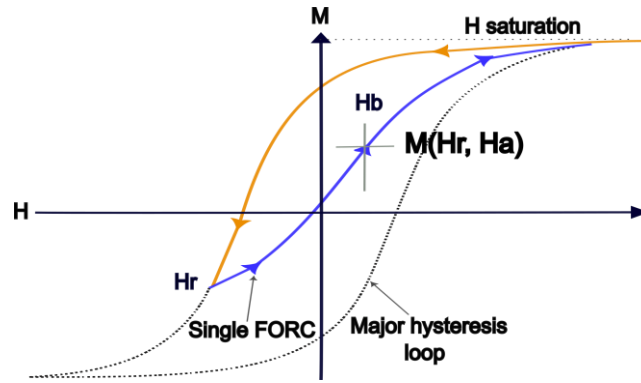
Figure 6. Representation of the acquisition of a single FORC. Orange line shows an initial magnetization phase, which subsequently reduce the external magnetic field from H saturation to Hr. Next, a blue line shows that the field is increased again to H saturation. Modified from Roberts et al. (2000).

The data obtained is presented in a FORC diagram. The FORC distribution, or M (Hr, Hb) is given by:

$$\rho(Hr, Hb) = \frac{\partial^2 M(Hr,Hb)}{\partial Hr \partial Hb)}, \text{ where Hr} < \text{Hb} \tag{18}$$

Generally, it is necessary to change the coordinates to represent a FORC diagram, which is given by $H_U = (H_b+H_r)/2$ y $H_C = (H_b-H_r)/2$. Being H_U and H_C the vertical and horizontal axes respectively. Since Hr < Hb, then $H_C>0$ and therefore the FORC diagram will be confined to the first quadrant of the Cartesian plane (the quadrant where all coordinates are >0). H_U is known as the microcoercivity (Roberts et al., 2000).

3.3. Paleosecular Variation (PSV) and Time Average Field (TAF)

The first relevant paleomagnetic studies that legitimized the GAD hypothesis were carried out on marine sediments by Opdyke & Henry, (1969) and on volcanic rocks by Wilson (1970, 1971). The GAD hypothesis is essential for paleosecular variation (PSV) and Time Average Field (TAF) models.

PSV studies describe the relative dispersion of VGPs with respect to the axis of rotation of a group of paleomagnetic sites in a defined region. The different models, both statistical and empirical, of PSV have provided information related with the expected field behavior for a GAD configuration (e.g. Baag & Helsley, 1974; Cox, 1970; Creer et al., 1959; Irving & Ward, 1964; McElhinny & McFadden, 1997; Tauxe & Kent, 2004).

The first two models (model A and B) to study secular variation just took account

of the dipole wobble. These two models in alphabetic order were published by Creer et al. (1959) and Irving & Ward (1964) respectively. While there is no doubt of the validity of A and B models, it is necessary to remember that only the dipole field is not adequate to represent the magnetic field. Advanced and more recently studies took account of dipole and non-dipole contributions. These studies in chronological order are: Model C, Model E, Model F and Model G, being published by Cox, (1970), Baag & Helsley, (1974), McFadden & McElhinny, (1984) and McFadden et al. (1988), respectively. The model G (Mcfadden et al., 1988) is the most widely accepted and projects a link to the description of spherical harmonics. In the G model, the quadrupole component is constant with latitude, but the dipole component is linearly dependent on latitude (Johnson & McFadden, 2015).

Another model with great acceptance is the TK03 (Tauxe & Kent, 2004). This model is substantiated on the statistical variability of each Gauss coefficient taking into account a spherical harmonic analysis. The TK03 model contains the basis of the Constable & Parker, (1988) model, which predicts a slight increase in the dispersion of the VGPs, putting less weight on to the axial dipole and adjusting the power spectrum in the asymmetric Gaussian coefficients.

TAF studies, on the other hand, provide details of the characteristics of the Earth's magnetic field such as the nature of magnetic deviations (non-GAD structure), internal processes of the Earth and the stationary geometry related to GAD (Johnson & McFadden, 2015). The TAF can be described and modelled as a representation of the spherical harmonics. Johnson et al. (2008) shows that this kind of studies work for stable polarities, focusing mainly on the last 5 Ma. The feasibility of TAF studies in this time interval is due to the large number of global data as well as relative non-huge tectonic changes. Generally, TAF is represented for about 95% by the dipolar component and the rest by the non-dipolar components. However, it may vary slightly from study to study (Hatakeyama & Kono, 2002; Mcelhinny et al., 1996; Merrill & McFadden, 2003).

A reliable paleomagnetic study of PSV and TAF should (i) recover primary remanence; (ii) have a number of temporarily independent sites that covers at least a period of 104 years; (iii) have multiple samples per site, in order to assess the error within each site; (iv) have not suffered the effects of tectonic movements since the acquisition of magnetic remanence.

3.3.1. (PSV) and (TAF) estimates

The equation given by (Cox, 1970), relates the total angular VGP dispersion (S) of a set of N sites with VGP determinations::

$$S = \left(\frac{1}{N-1}\sum_{i=1}^{N}\Delta_i{}^2\right)^{\frac{1}{2}},$$ (19)

where Δ_i is the angular distance between VGP and the mean of the dataset. The next step is to remove random errors associated with sampling and the quality of the measurements (Doell, 1970). McElhinny & McFadden, (1997) shows the following equation to get only the dispersion associated with the magnetic field, and minimising the errors.

$$S = \left(S^2 - \frac{S_w{}^2}{n}\right)^{\frac{1}{2}}$$ (20)

Where n is the number samples from one site to another. To retain consistency with past studies (e.g. McElhinny & McFadden, 1997), the error term (correction factor "$\frac{S_w{}^2}{n}$") using the α95 (95% confidence related with the paleodirections distribution) for a certain set of data is estimated using:

$$\frac{S_w{}^2}{n} = 0.335\alpha_{95}^{-2}\frac{(1+3sin^2(\lambda))^2}{(5+3sin^2(\lambda))},$$ (21)

where λ is paleolatitude.

On the other hand, the TAF direction is usually studied in terms of its GAD deviations (Cox, 1975). It is helpful to convert deviations from GAD directions as inclination anomalies. Therefore, the inclination anomaly (ΔI) is defined as follows:

$$\Delta I = I_{obs} - tan^{-1}(2tan\,\lambda),$$ (22)

where I_{obs} is the observed site inclination and $(tan^{-1}(2tan\,\lambda))$ is the I_{GAD}. It is essentialy the inclination predicted by the GAD field, where λ is the site latitude. All the reverse polarity data are inverted to obtain normal polarity equivalents.

In order to obtain the non-dipole contributions (quadrupole ($G2 = g_2^0/g_1^0$) and octupole ($G3 = g_3^0/g_1^0$) components), we use an equation developed originally to estimate the poles from oceanic plates (Gordon & Cox, 1980). The equation given by McElhinny et al. (1996) is defined as follows:

$$tan(I_{obs}) = \frac{2\cos\theta + G2(\frac{9}{2}\cos^2\theta - \frac{3}{2}) + G3(10\cos^3\theta - 6\cos\theta)}{\sin\theta + G2(3\cos\theta\sin\theta) + G3(\frac{15}{2}\cos^2\theta\sin\theta - \frac{3}{2}\sin\theta)},$$ (23)

where g_1^0 is the axial dipole term, and θ is the colatitude (90° − latitude).

3.4. Excursions

The Earth's magnetic field presents geomagnetic inversions and excursions, which are variations of greater amplitude and duration. These phenomena are strongly influenced by lateral variations on the inner mantle-outer core boundary (Glatzmaier & Roberts, 1997).

The time intervals in which the magnetic field is predominantly the same polarity (approximately >1 Ma) is called chrons. Usually, within these chrons, the magnetic field reverses its polarity in a very short time interval (<0.1 Ma), these have been called subchrons. The last predominant reversion in the Earth's magnetic field occurred 0.78 Ma ago. The key difference between excursions and geomagnetic secular variation is that secular variation has the colatitude ("θ") lower than 45° (Merrill et al., 1998).

Excursions are short-lived ($<10^3$ years) deviations of the virtual geomagnetic pole (VGP) from the geocentric axial dipole (GAD), which lie outside the range of secular variation for a particular population of VGPs (Laj & Channell, 2007; Merrill & McFadden, 2003). The question of the origin of the excursion are still open, but it is usually connected to a collapse of the geomagnetic field being systematically accompanied by very low intensities (Roberts, 2008).

There are multiple hypothesis related with geomagnetic excursions. Excursions occur due to large amplitude changes in the secular variation, which are either failed reversals or, instead, chaotic behavior in the nonlinear system of equations that govern the magnetic field (Merrill & McElhinny, 1983). In addition, Gubbins, (1999) suggested that Earth's inner core could stabilize the magnetic field. The inner core is solid and changes in the field can only take place by electrical diffusion (in a relative period of 3 ka). From this perspective, excursions occur when the magnetic field in the outer core (liquid) reverses its polarity (in a relative period of 0.5 ka), but the inner core does not follow this polarity reversal.

A complete reversal only occurs when the reversion in the outer core persists long enough for the field in the inner core to completely change its polarity. As a consequence, the integral reversal of the magnetic field is retarded by the inner core of the Earth. In this time, the previous polarity configuration in the outer core can be restored. However, exact duration of the geomagnetic excursions remains contentious (Roberts, 2008).
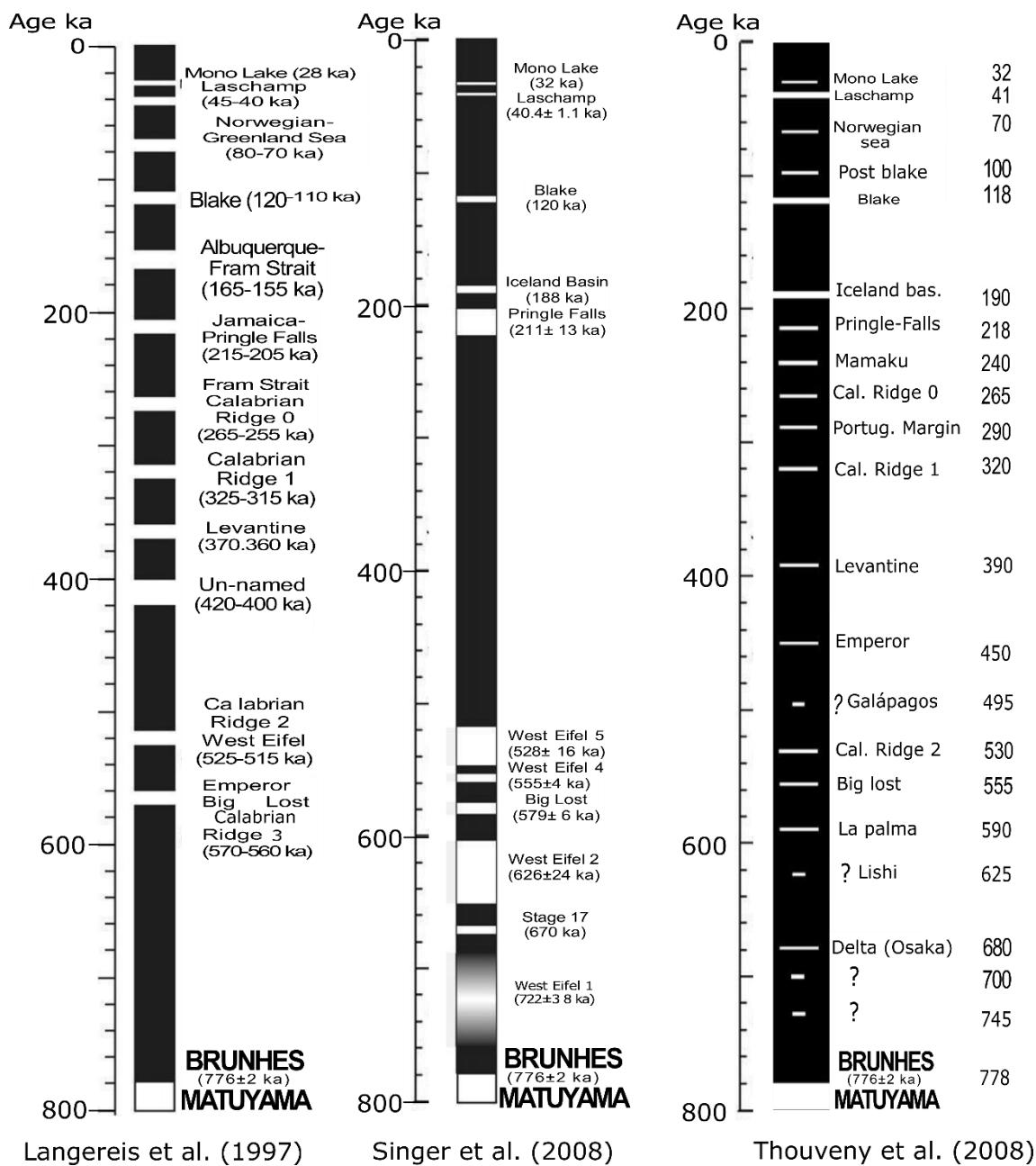
Figure 7. Records of geomagnetic instabilities (excursions) which took place in the Brunhes epoch. Records are from: (C. G. Langereis et al., 1997; Singer et al., 2008; Thouveny et al., 2008).

METHODS

4. METHODS

4.1. Fieldwork

A total of 247 samples were collected from 23 sites throughout the Southern part of Ecuador (Figure 1, 8). The samples were collected with a water-cooled, gasoline-powered drill Pomeroy magnetic oriented equipped with a Brunton compass (figure 8c) was used for orienting the drill cores. Drill cores were cut into specimens approximately 2.2 cm in length.

4.2. Laboratory work

All measurements were performed in the Laboratory of Paleomagnetism at the University of São Paulo (USPmag). Susceptibility, Anisotropy of Magnetic Susceptibility (AMS) and temperature dependent susceptibility from selected samples were obtained using a Kappabridge KLY4 coupled with a CS3 furnace (Figure 9a), in order to fully characterize magnetic signature and behavior of the main carriers of magnetization in the samples (e.g. Curie temperature, type of magnetic minerology, etc). AMS data, internal dispersion, shape and anisotropy degree were analyzed using the Anisoft5 software (Hrouda & Schulmann, 1990) using the statistics of Jelínek, (1978).

All hysteresis (magnetic field versus magnetization) analysis, First-Order Reversal Curve (FORC), Isothermal Remanent Magnetization (IRM) and their combinations (Mrs/Ms; Bcr/Bc) were carried out using a Princeton Measurement Corporation Micromag vibrating sample magnetometer (VSM) (Figure 9b). These experiments were performed on small pieces of rocks. The importance of (Mrs/Ms; Bcr/Bc) to get a Day plot lies in analyzing the magnetic domains (grain size parameters) (Day et al., 1977; Dunlop, 2002) such as superparamagnetic (SP) (i.e. 0.03 μm for hematite and magnetite), single domain (SD), multi domain (MD), and pseudo-single domain (PSD) or vortex state.

Figure 8. Examples of sampled outcrops of all volcanoes studied from Southern Ecuador: a) Sagoatoa summit lava flow with sample site SE01 shown. b) Another outcrop of Sagoatoa volcano showing a distal lava flow, at the west of Píllaro city and covered by the Chalupas ignimbrite. c) Taking sun readings at the brecciated lava flow located at the north flank of the Huisla-Mulmul volcanic complex, with sampling site SE04 shown. d) Fresh and distal lava flow of Igualata volcano, sampling site SE09, under Mulmul lava flow. e) Distal lava flow of Calpi cone covered by the DAD of Chimborazo. f) Lava flow of Licto cone located at Cerro Tulubug with sample site SE15. g) Chimborazo distal lava flow with sample site SE21. h) Chimborazo distal and weathered lava flow with sample site SE22.

A JR6 Dual Speed Spinner Magnetometer (Figure 9c) was used for all the paleomagnetic measurements. A total of 196 specimens from all sites were subjected to stepwise demagnetization using both an AF (alternating field) demagnetizer LDA-5

AGICO (Figure 9d) and a thermal demagnetizer TD48SC ASC-Scientific (Figure 9e). The paleomagnetic vector directions were retrieved using the principal component analysis (PCA) method (Kirschvink, 1980) and directional statistics (Fisher, 1953). Finally, the paleomagnetic results were used to calculate the he virtual geomagnetic poles (PSV), the TAF and PSV parameters, which were then compared with available paleosecular models (e.g. model G, TK03). For the analysis, the paleomagnetic data must fulfill the following requirements: (1) at least 5 samples per site and (2) a Fisher precision parameter ≥ 100 (Tauxe et al., 2003).
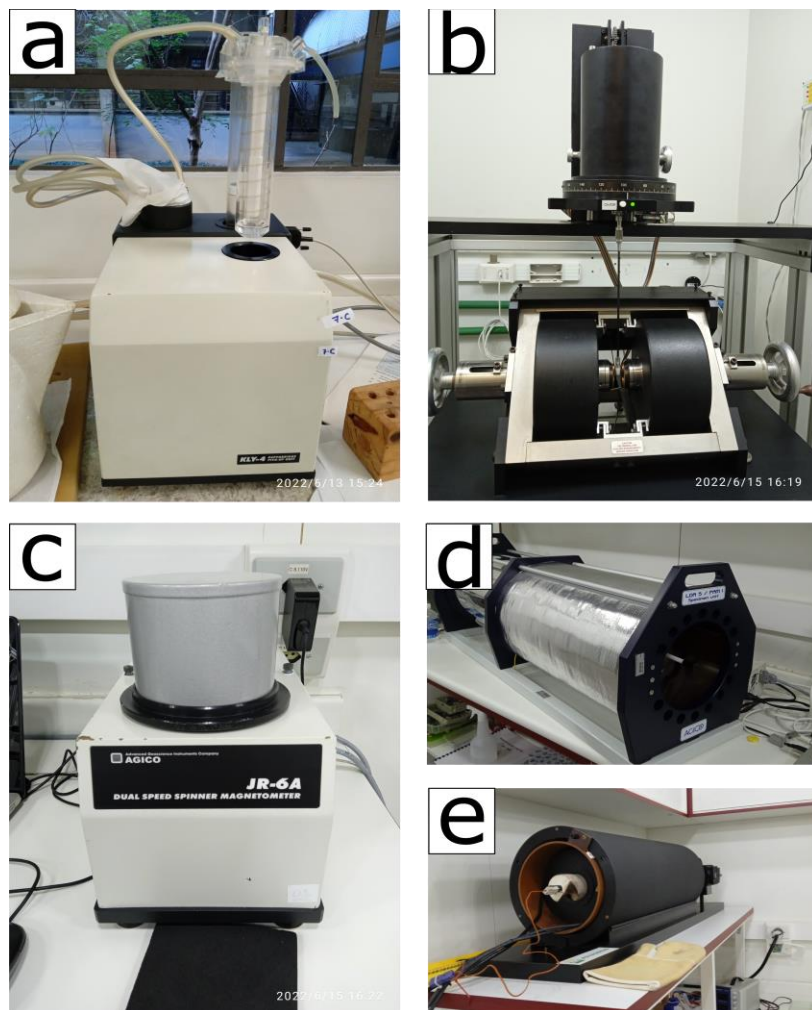
Figure 9. Laboratory equipment used in this work. a) Photo of the Advance Geoscience Instrument Company (AGICO) susceptibility meter, model KLY4. b) Photo of the Princeton Measurement Corporation Micromag vibrating sample magnetometer (VSM) c) Photo of a JR-6A Dual Speed Spinner Magnetometer. d) Photo of the AF demagnetizer LDA-5. e) Photo of a thermal demagnetizer TD48SC ASC-Scientific.

.

RESULTS AND INTERPRETATION

5.   RESULTS AND INTERPRETATION

5.1. Rock Magnetism

5.1.1. Thermomagnetic analysis

Thermomagnetic curves (susceptibility vs temperature) from each volcanic edifice from southern Ecuador are shown in Figure 10.

Low-temperature experiments were performed after insertion of samples in liquid nitrogen (from -194 to 0.5) and subsequent heating. The curves show an initial abrupt increase in susceptibility for all samples (Figure10 a, c, e, f), except for sample SE03 (Figure 10b) belonging to Huisla Mulmul (Group I) and sample SE09 (Figure 10d) belonging to Igualatá volcano. The Verwey transition at around -150°C (Verwey, 1939) is clearly detected in SE01 (sample belonging to Sagoatoa) and SE23 (sample belonging to Carihuairazo). However, this peak is attenuated in SE03 and in SE18. The Verwey transition evidence the transformation of magnetite crystalline symmetry in heating, from monoclinic to cubic (Verwey, 1939). Samples from Igualatá volcano (SE03) and from from Huisla Mulmul (Group II, SE06) do not show Verwey transition.

High-temperature experiments yield a representative phase of titanomagnetite with variable amounts of titanium, displaying a nearly reversible behavior except for samples from Calpi cone (Figure 10c), which show less degree of reversibility. Volcanoes from Southern Ecuador show two main thermomagnetic behaviors according with their Curie temperature (Figure 10). The first one corresponds to Curie temperatures in the range of 533°C to 560°C (Figure 10a-d and f) with an average around 549°C and a standard deviation of 8.7. This Curie temperature range suggests that Ti-poor titanomagnetite (e.g., Dunlop & Özdemir, 1997) is the main carrier of magnetization for all the volcanic edifices studied, except for Calpi and Licto cones. The second thermomagnetic behavior comprises the two samples from Calpi and Licto cones, displaying a Curie temperatures in the range of393°C to 490°C (Figure 10e), which suggest that Ti-rich titanomagnetite is the main carrier of magnetization in these rocks.

Thermomagnetic curves from Sagoatoa (Figure 10a), Igualatá (Figure 10d) and Carihuairazo volcanoes (Figure 10f) exhibit a hump between 105°C to 400°C. Johnson & Merrill, (1972) explained this rounded lump as the inversion of maghemite, which occurs in this range of temperature. On the other hand, Sagnotti, (2007) explained this hump as negligible amounts of pyrrhotite. Thermomagnetic behavior for all the volcanoes from

Southern Ecuador display a sharp pronounced peak (increase in susceptibility with different slopes) before transition. This effect is named as Hopkinson peak. While no meaningful hematite is perceived on this thermomagnetic curves, some tails related with hematite are seen in temperatures $\geq$ 590 °C (e.g. Huisla Mulmul sample, SE03; Figure 10b).
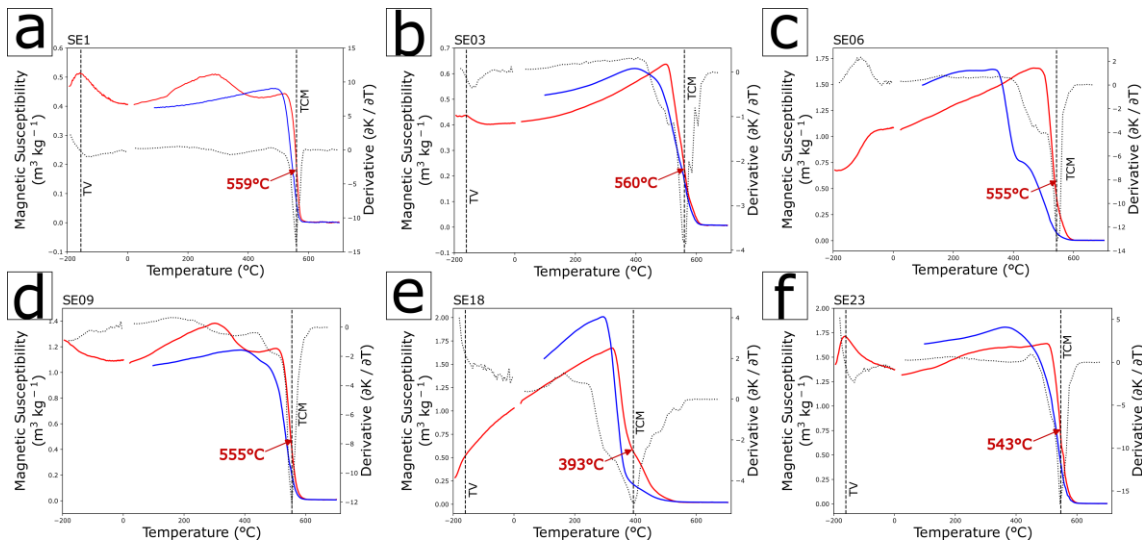
Figure 10. Representative thermomagnetic (susceptibility vs temperature) curves from (a) SE1-Sagoatoa volcano; (b) SE03-Huisla Mulmul (Group I); (c) SE6-Huisla Mulmul (Group II); (d) SE9-Igualatá volcano; (e) SE18-Calpi cone; (f) SE23-Carihuairazo volcano. The heating curves are shown in red and the cooling curves are shown in blue. Dashed black lines are the derivate associated to the heating curve; TV is Transition of Verwey, and TCM: Temperature Curie Magnetite.

5.1.2. Hysteresis curves and FORC diagrams.

Hysteresis and FORC diagrams were performed for one sample per site. Based on the hysteresis parameters, saturation magnetization (Ms), saturation of remanent magnetization (Mrs), coercivity (Hc), and remanent coercivity (Hcr), we constructed a Day plot for all analysed samples (figures 11 and 12). In these plots we represent the Mrs/Ms ratio against the Hcr/Hc ratio (Day et al., 1977). Results obtained for our samples, show that the majority of the volcanoes lies within the main PSD region (Figure 11a) with exception of 4 samples. Those 4 samples are shifted to the right, indicating most likely the existence of a combination of SP, PSD and MD particles in distinct percentages. Group I and II from Huisla Mulmul are in the PSD range, being slightly shifted to the right (red squares enclosed in a red dashed circle).

Representative hysteresis loops show graphically different grain size distributions along the whole Ecuadorian southern termination arc (Figure 11b-i). Seven samples have near typical SD hysteresis loop (e.g. Figure 11b, and c), being shifted to the left in the Day plot and close to the SD region. Eleven samples have higher Hcr/Hc ratios than the seven samples before. Those eleven samples are in the range (2.53 – 4.2) and reflect typical hysteresis curves that are indicative of PSD (e.g. Figure 11d, h, i). In contrast, hysteresis loops and Day plot from samples SE01, SE15, and SE23l reveal its multidomain character (e.g. Figure 11f), being supported by the Day plot.

Hysteresis loops for samples from Chimborazo volcano (SE19 and SE21; Figure 11e) and one sample from Calpi cone (SE18; Figure 11g) have a wasp waisted shape and low Hc values (8.2, 7.8, and 9.4 respectively; Supplementary 1), proving possibly the presence of multidomain (MD) magnetite, contributing therefore with two magnetic components with different coercivities (e.g. Wasilewski, 1973). Superparamagnetic contribution for Chimborazo samples could be perceived but in small percentage, which also could produce wasp waisted shapes from the combination of SD and SP behaviors (Jackson et al., 1993; Tauxe et al., 1996).
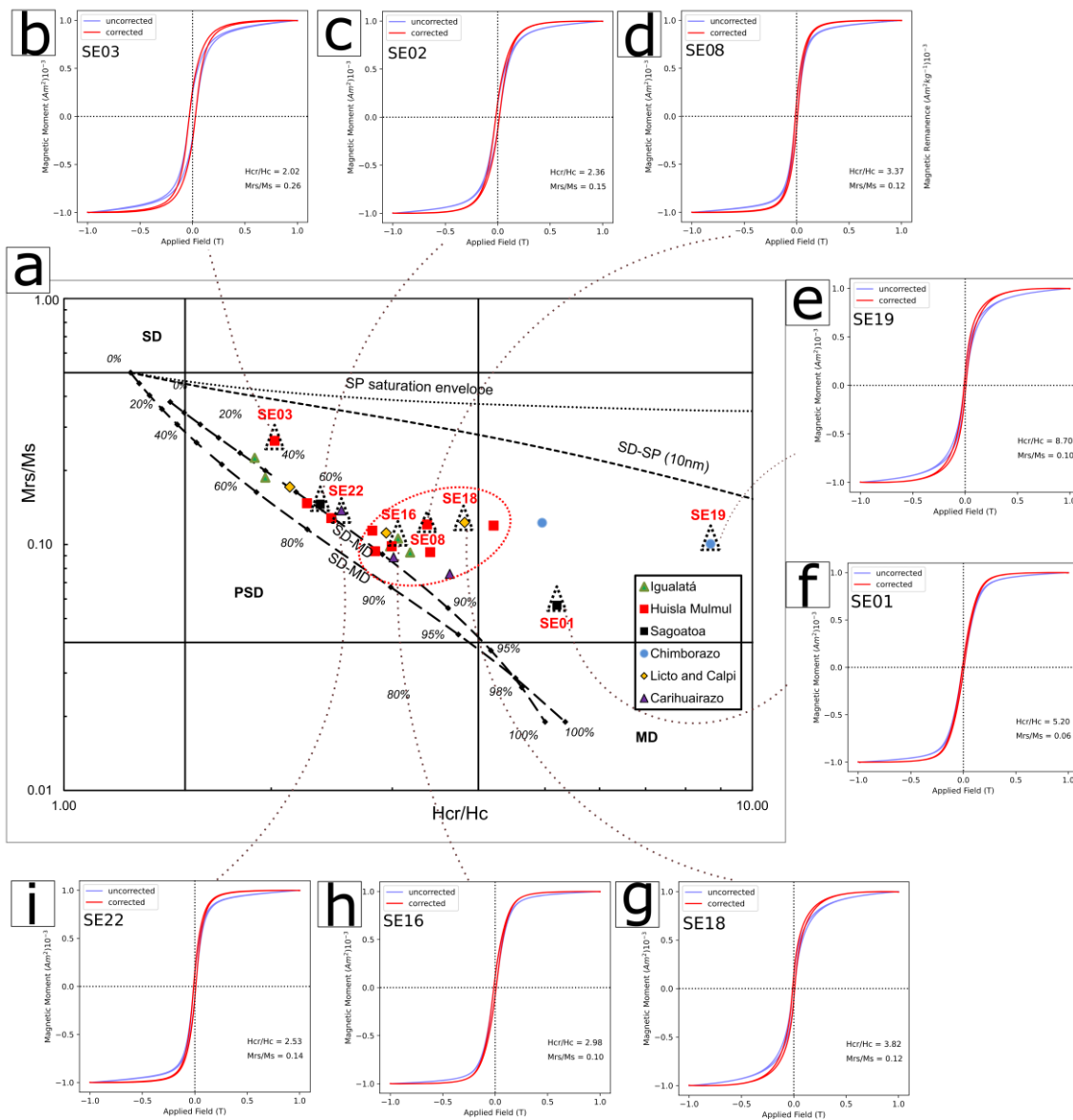
Figure 11. Magnetic hystereis curves and parameters from the volcanoes belonging to Southern Ecuador. a) Day diagram for all the sites (Day et al., 1977). Mrs/Ms: remanent saturation magnetization/saturation magnetization; Hcr/Hc: remanence coercivity/coercivity. Super paramagnetic (SP), single domain (SD), pseudo-single-domain (PSD), and multidomain (MD) grains areas are indicated by the solid lines (Dunlop, 2002); note the percent of MD marked within the mixture models. Magnetic hysteresis loops from (b) Huisla Mulmul (Group I-SE03); (c) Sagoatoa (SE02); (d) Huisla Mulmul (Group II-SE05), red dashed circle represents the samples belonging from Huisla Mulmul group II; (e) Chimborazo (SE19); (f) Sagoatoa (SE01); (g) Licto and Calpi (SE18); (h) Igualatá volcano; and (i) Carihuairazo volcano (SE22).

FORC diagrams and IRM acquisition curves are shown for four representative samples (Figure 12). These FORC diagrams show a gradual change in the FORC distribution from nearly SD (Fig. 12b and e) to PSD (Fig. 3c and d). FORC diagrams of samples SE20 and SE03 display distinct closed-contour peaks between 0.016 and 0.035 T respectively in the FORC distribution. SE3 sample (Figure 12b) has nearly symmetrical inner contours, slightly non symmetrical outer contours and a bigger coercivity elongation (from 0.03 to 0.06 T), suggesting a large fraction of isolated, non-interacting particles. SE20 sample (Figure 12e) shows smaller coercivity elongation, suggesting more interacting particles in this sample. Both samples display a predominant SD behavior for magnetite (e.g., Roberts et al., 2000), having a prevalence of low coercivity components. FORC diagrams of SE02 (Figure 12c) and SE09 (Figure 12d) display an asymmetrical shape, having a broad vertical distribution along Bu axis, albeit with the existence of a central ridge, a behavior that characterizes the PSD. The main coercivity peak is located between 0.014 T and 0.018 T with tail reaching up to 0. 12 T.

Stepwise IRM acquisition curves from almost all sites show a rapid rise in magnetization, reaching more than 90% of the saturation isothermal remanent magnetization (SIRM) between 0.1 T to 0.25 T and about 98% between 0.25 to 0.3 T (Figure 12 b-e). The data obtained corroborates the dominance of low-coercivity minerals in these samples (likely magnetite with varied amounts of Ti, and/or maghemite). Four samples are the exception to this behavior, among which are SE18 (Calpi), and two samples from Chimborazo volcano (SE19 and SE21). Those samples show two markedly different slopes. The first pronounced slope reaches 60% to 68% of the SIRM at 0.09 T, and the second slope reaches complete saturation at 0.4 T. The first slope is associated with low coercivity minerals, whereas the second slope likely arises from small proportions of hematite and/or goethite ("hard" magnetic minerals). It means that the last behavior shows bimineralic specimens containing both low and high coercivity magnetic mineralogy.
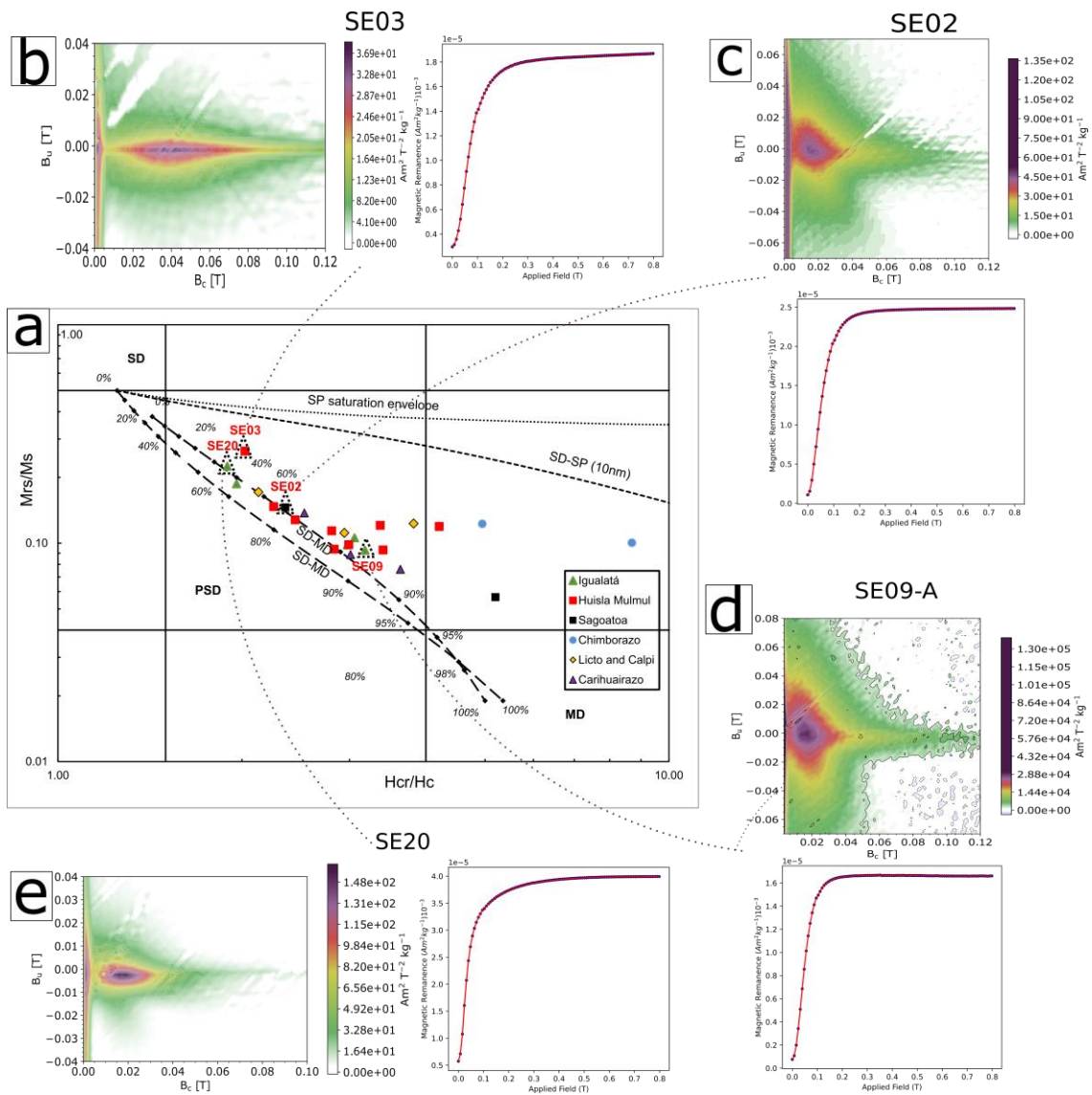
Figure 12. Representative FORC diagrams, Isothermal remanent magnetization IRM acquisition curves, and Day plot from Southern Ecuador. a) Day plot for all the sites (Day et al., 1977). FORC diagrams and IRM acquisition curves from some volcanoes of southern Ecuador: b) SE03 (Huisla Mulmul); c) SE02 (Sagoatoa volcano); d) SE09 (Igualatá volcano); and SE20 (Igualatá volcano).

5.2. Anisotropy of Magnetic Susceptibility (AMS)

Based on the mean magnetic susceptibility (Figure 13a), the average from all volcanoes is 0.023263 ±0.00704 SI. Specifically, the Igualatá volcano shows a bi-modal arrangement, with the first distribution between 1.0 and 1.7 (10^{-2} SI), and the second distribution between 1.7 and 3.0 (10^{-2} SI). The lowest susceptibility range belongs to SE20 and SE14 sites, while the highest values related to SE09, SE13 and SE16 sites. Huisla

Mulmul volcanic complex shows a normal distribution, with Group I being less magnetic (peak ar $1.7*10^{-2}$ SI) and Group II showing the highest magnetic susceptibility of all volcanoes from this study, with a peak at $3.3*10^{-2}$ SI. Both sites from Carihuairazo have different behavior. SE22 is less susceptible and has a wide distribution from 0 to $2.3*10^{-2}$ SI, while SE23 has higher susceptibility, but restricted to a limited range of 2.3 to $2.8*10^{-2}$ SI.

The mean degree of anisotropy (P) from the volcanic rocks of southern Ecuador studied here is relative low, with an average P value of 1.0260 ± 0.015 (Figure 13b). The degree of anisotropy for all lava flows are between 0.5%-8%, which are typical values of lava flows from previous studies (e.g. Atarita et al., 2019; Desi Wulan Ndari et al., 2020). A low P parameter ($\leq 8\%$) indicates a syn-magmatic flow fabric as emplacement mechanism of for all lava flow (Henry, 1988). Generally, there is not an apparent correlation between the mean susceptibility vs the degree of anisotropy for the volcanoes, but also these values do not present important difference between each volcanic edifice. Although, Chimborazo volcano shows possibly a direct correlation between the mean susceptibility vs the degree of anisotropy. Carihuairazo volcano has the lowest values of the degree of anisotropy, being their samples more isotropic than other volcanoes from southern Ecuador. The highest values related with the degree of anisotropy belongs to one site from Igualatá volcano (SE16).

Shape parameter is essential to characterise if the sample is oblate or prolate. A consistent relationship is not clear among the different volcanoes studied. SE06, SE09, SE10, SE15, SE16, SE19 sites are mainly oblate and only two sites (SE01, and SE05) have ellipsoids that are mainly prolate, while the other 15 sites do not show a clear tendency (Figure 13c). Finally, the magnetic foliation (F = k2/k3) and the degree of anisotropy (P = k1/k3) shows a direct relationship. As the degree of anisotropy increases, the magnetic foliation also increases (Figure 13d), the sample with the highest values of magnetic foliation also presenting the highest degree of anisotropy (sites SE16 "Igualatá" and SE19 "Chimborazo").
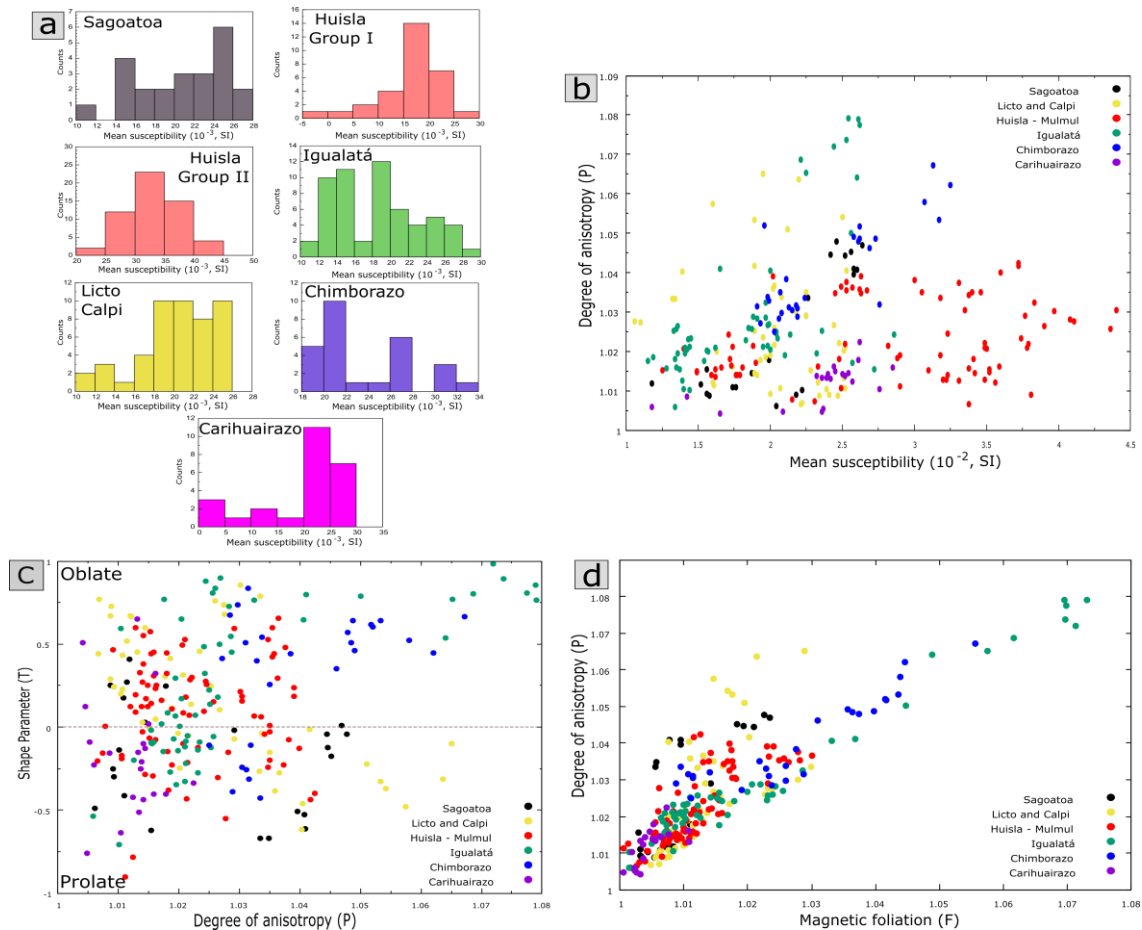
Figure 13. AMS measurements to analyse the respective fabric type and differentiated by each volcanic edifice: a) Histograms of the Mean susceptibility vs the occurrence; b) a plot of the mean susceptibility vs degree of anisotropy (P); c) a plot of the corrected degree of anisotropy (P) vs shape factor (T) (Jelínek, 1981); and d) magnetic foliation (F) vs degree of anisotropy (P) for all sites.

AMS magnetic fabric can be divided into normal, intermediate and reverse (Figure 14). A normal coaxial magnetic fabric has a magnetic lineation ($k1$) parallel to the lava flow direction. In addition, the k3 (the pole of the magnetic foliation) is expected to lie normal to the flow plane (Rochette et al., 1992). Normal magnetic fabric is the predominant feature in the studied lava flows, being found in almost all volcanoes, except in the Sagoatoa volcano (Figure 15; e.g. SE05, SE06, SE10, SE11, SE12, SE13, SE16, SE19, SE20, SE21, SE22). The second most abundant magnetic fabric from Southern Ecuador is the inverse. An inverse magnetic fabric occurs when the magnetic foliation is perpendicular to the expected magmatic flow plane (Ferré, 2002; Rochette et al., 1992). For example, this feature is recognized in SE02, SE07, SE17 and SE23, belonging to Sagoatoa, Huisla-Mulmul, Licto and Carihuairazo volcanoes respectively. SE01 is the unique site that shows and intermediate

magnetic fabric (Figure 15).
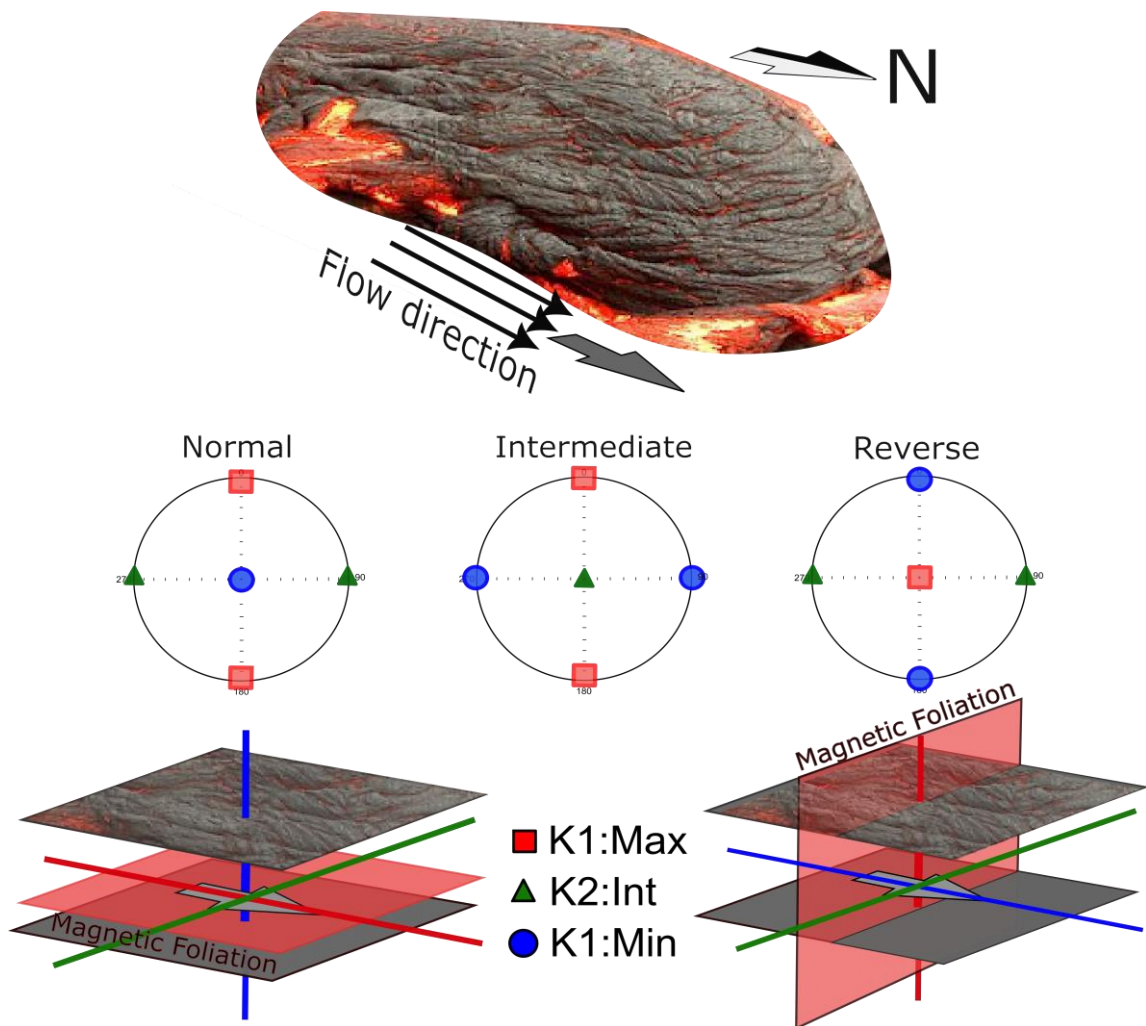
Figure 14. Normal, intermediate and inverse magnetic fabric taking account the magma flow direction. Principal magnetic axes from a lava flow are showed in a lower hemisphere Schmidt net. Where a red square is the k1, a green triangle is the k2, and blue circle is the kmin. Modified from Schöbel & de Wall (2014).

In order to analyze the magnetic fabric for all lava flows, an analysis of the three principal axes k1, k2, and k3 was made for all sites with normal fabric. For this analysis, the eigenvectors were plotted at the equal-area stereographic projection (Jelínek, 1978). Although the direction of the magnetic lineation (k1) has been used as an indication of flow direction by several authors (e.g. Cañón-Tapia et al., 1997; Herrero-Bervera et al., 2002; Ort et al., 2003), recent work has shown that the orientation of k3 is a more robust indicator (e.g., Hillhouse and Wells, 1991; Giordano et al., 2008; Dedzo et al., 2011; Haag et al., 2021). In the later case, the flow direction is estimated by the imbrication of magnetic grains, resulting

in a k3 tilted towards the magmatic flow direction (Giordano et al., 2008; Gambeta et al., 2021; Haag et al., 2021). Thus, the normal to magnetic foliation in AMS plots is used to infer flow directions (figures 14 and 15).
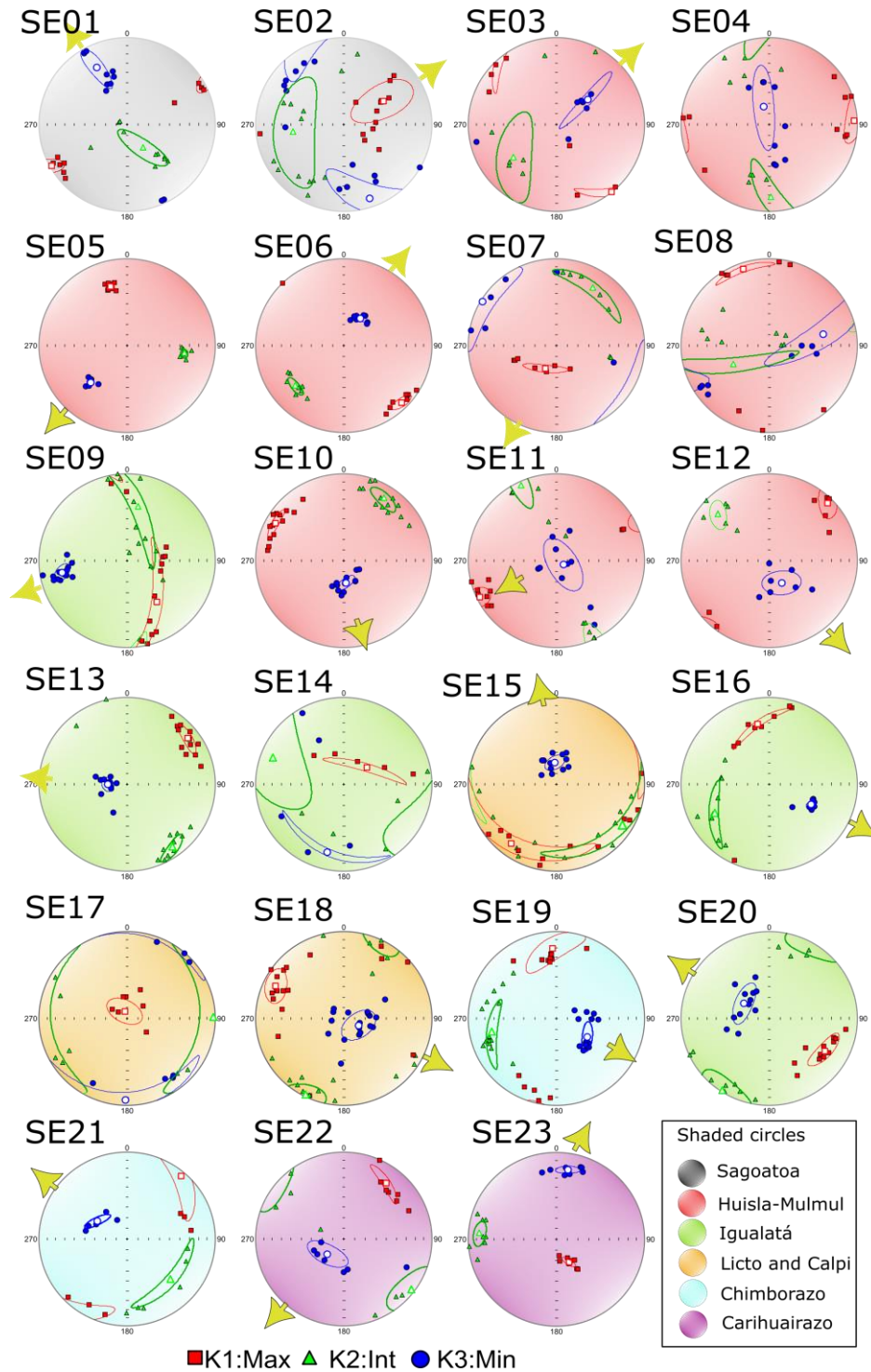
Figure 15. AMS directions for all sites in this study. Red square is k1, green triangle is k2, and blue circle is k3. The yellow arrows correspond to the magnetic lineation direction,

which is parallel to the magma flow direction.

Table 2. AMS results for all lava flows. n = number of samples; Km = mean magnetic susceptibility (10−2 SI); k1 or kmax, k2 or kint and k3or kmin; E1-2 and E1-3: confidence ellipses; Pj = degree of anisotropy; T = shape parameter. Data on (parenthesis) is standard deviation.

Site ID	Location		n	K_m	K_1	K_2	K_3	E_{1-2}	E_{1-3}	Pj	T
	Longitude	Latitude		(10−2 SI)	(D / I)	(D / I)	(D , I)				
Sagoatoa											
SE01	-1.15216	-78.66460	9	2.47 (0.18)	(240.4/5.5)	(141.7/57.7)	(333.8/31.7)	9.6/5.1	24.4/5.3	1.043 (0.003)	-0.336 (0.284)
SE02	-1.17572	-78.56832	11	1.78 (0.32)	(57.6/54.4)	(244.6/35.4)	(152.2/3.3)	20.3/12.4	40.4/13.0	1.012 (0.003)	-0.097 (0.345)
Huisla-Mulmul											
SE03	-1.3748	-78.57121	8	1.22 (0.59)	(132.5/9.5)	(227.7/28.5)	(25.9/59.7)	1.2/1.1	1.7/1.1	1.018 (0.005)	-0.072 (0.175)
SE04	-1.41314	-78.53966	9	3.49 (0.19)	(87.2/4.4)	(178.5/16.7)	(343.1/72.7)	17.4/9.5	41.1/9.4	1.026 (0.012)	-0.041 (0.344)
SE05	-1.42084	-78.54192	8	3.15 (0.33)	(344.3/30.2)	(98.2/34.7)	(224.5/40.5)	4.0/2.9	3.6/3.0	1.036 (0.002)	-0.093 (0.116)
SE06	-1.42442	-78.54524	8	2.53 (0.21)	(135.0/8.1)	(229.4/28.5)	(30.6/60.2)	8.6/5.0	5.9/3.1	1.038(0.001)	0.399 (0.145)
SE07	-1.43024	-78.54848	8	2.41 (0.13)	(189.2/62.8)	(24.3/26.4)	(291.2/6.1)	21.0/9.9	23.5/11.2	1.017 (0.011)	0.101 (0.322)
SE08	-1.35934	-78.56045	8	3.62 (0.31)	(341.6/8.1)	(241.2/51.7)	(77.7/37.1)	22.3/3.6	62.1/10.5	1.023 (0.005)	0.147 (0.424)
SE10	-1.38589	-78.583294	13	1.70 (0.12)	(299.0/12.2)	(32.7/16.7)	(174.7/69.1)	11.6/4.0	9.8/4.2	1.016 (0.002)	0.304 (0.129)
SE11	-1.393152	-78.580527	12	3.19 (0.26)	(248.4/2.8)	(338.4/1.7)	(99.1/86.7)	17.3/11.4	33.1/15.8	1.015 (0.004)	-0.216 (0.369)
SE12	-1.394392	-78.577468	8	3.87 (0.43)	(48.6/3.4)	(317.2/22.2)	(146.7/67.5)	20.3/15.4	16.4/11.2	1.029 (0.004)	0.166 (0.207)
Igualata											
SE09	-1.46754	-78.51706	15	1.93 (0.14)	(135.9/47.2)	(3.0/32.2)	(256/24.9)	64.3/6.1	13.1/8.0	1.030 (0.007)	0.557 (0.328)
SE13	-1.4916	-78.61761	12	2.15 (0.42)	(52.3/14.4)	(145.1/10.5)	(269.9/72)	12.9/5.3	6.9/5.3	1.021 (0.003)	0.013 (0.132)
SE14	-1.49372	-78.64052	7	1.34 (0.14)	(93/49.3)	(248.7/38)	(348.4/12.2)	51.3/25.7	59.3/27.9	1.017 (0.006)	0.032 (0.486)
SE16	-1.636359	-78.570134	9	2.48 (0.16)	(349.2/30.1)	(240.7/28.7)	(116.2/46)	30.3/3.1	4.8/3.1	1.077 (0.011)	0.801 (0.122)
SE20	-1.55601	-78.683621	13	1.38 (0.03)	(124.8/27.4)	(34.1/1.3)	(301.5/62.5)	22.5/8.2	18.2/8.3	1.020 (0.005)	-0.024 (0.274)
Licto and Calpi cones											
SE15	-1.78668	-78.60673	12	2.28 (0.21)	(216.9/15.6)	(123.3/12.6)	(356.1/69.7)	66.5/9.1	10.0/6.0	1.01 (0.002)	0.477 (0.206)

SE17	-1.63993	-78.72759	8	1.49 (0.40)	(357.5/82.1)	(97.8/1.4)	(188.0/7.7)	17.4/11.9	63.0/9.7	1.045 (0.015)	0.054 (0.585)
SE18	-1.64961	-78.74456	22	2.16 (0.23)	(294.8/13.4)	(26.4/6.7)	(142.5/75.0)	14.8/13.7	22.2/12.5	1.030 (0.011)	0.066 (0.352)
Chimborazo											
SE19	-1.60181	-78.66749	16	2.59 (0.44)	(3.1/17.4)	(264.0/26.8)	(122.2/57.2)	38.4/12.1	13.9/6.7	1.049 (0.012)	0.528 (0.209)
SE21	-1.50261	-78.7297	6	2.01 (0.06)	(40.2/5.6)	(133.8/32.0)	(301.4/57.4)	39.3/9	13/3.5	1.031 (0.004)	0.362 (0.271)
Carihuairazo											
SE22	-1.37637	-78.65044	7	1.37 (0.89)	(42.7/22.8)	(312.4/0.7)	(220.8/67.2)	12.9/5.3	15.5/5.0	1.005 (0.001)	0.018 (0.463)
SE23	-1.33902	-78.71745	8	2.44 (0.09)	(151.8/65.6)	(274.1/13.6)	(9.2/19.8)	7.6/2.2	9.6/4.0	1.014 (0.001)	-0.169 (0.367)

AMS sites that exhibited high internal dispersion are SE02, SE08, and SE14 belonging to Sagoatoa, Huisla, and Igualatá volcanoes respectively (Figure 15). The northwest direction of SE01 k3 axes could record the initial flow direction of the Sagoatoa volcano at 826 ky, while the other site from this volcano (SE02) has a northeast trend. Both sites (SE10 and SE12; Figure 16a and b) founded at the southeast flank of the Huisla volcano have a southeast flow direction. The westernmost and the lava flow north of the Huisla crater (SE11 and SE03 respectively) display a northeast plunging k3 axes. In addition, the lava flow located on the north flank of the Mulmul volcano was not inferred, because dispersion in SE08 is high. Starting from northeast to southwest, sites around Huisla crater show a clockwise magnetic foliation rotation (Figure 16, e.g., from north to south: SE03, SE11, SE10, SE12). It starts from nearly vertical foliation (SE03) and finish to almost horizontal foliation (SE12). This volcano is interpreted as multiple lava flows, which were fed by a unique crater, and being those lavas successive deposited downhill towards the south. Both lava flows that are furthest north and south of Mulmul volcano (SE05 and SE07; Figure 16a) display a southwest flow direction. In contrast, a lava flow at the middle of these sites (SE06) shows a flow direction towards the northeast. A high dispersion in SE04 is noted.

This high dispersion is noted also in a lava flow from Igualatá volcano (SE14 ≃ 376 ka) and could be due to proximity of the Igualatá crater, considering that the thermal effect from subsequent eruptions (SE13 ≃ 337 ka; SE16 ≃ 358 ka; SE20 ≃ 183 ka) could disturb the petrofabric arrangement. The remaining two lava flows on the Igualatá volcanic edifice (SE13 and SE20) exhibit a westward flow direction (Figure 15 and 16). A lava flow located southeast of the Igualatá shows also a southeast imbrication. Possibly, those lava flows exited the Igualatá volcano near SE13 and SE14 and travelled downvalley from there until at least reaching SE16 site. A northeast flank lava flow from Carihuairazo volcano (SE23) indicates

a northeast flow direction, being consistent even with topography, while the sample furthest from the crater (SE22) display an opposite flow direction (southwest).

Both sites from Chimborazo volcano have a magnetic foliation nearly vertical, however these lava flows 15 meters apart display a contrasting flow direction. SE19 indicates southeast flow direction, while an opposite imbrication from SE21 indicating a westward flow direction. A lava flow from Calpi cone (SE18) shows a vertical foliation pattern and a southeast flow direction. SE17 have typical PSD hysteresis loop and even with a high dispersion of SE17, it could be interpreted as feeder conduit zone, because of the morphology and flow direction. Finally, The imbrication of SE15 (Licto volcano) is inferred to be north direction and almost horizontal magnetic foliation.

Generally, lava flows from different volcanic edifices and emplaced in a wide area tend to show highly complex AMS patterns. Regionally, the magnetic foliation does not have any consistent regional pattern orientation, even the contemporaneous lava flows from the same volcano do not show any consistent pattern (Figures 15, and 16), except for specific case as Huisla and Igualatá volcanoes. The magnetic imbrication (Figure 15 and 16) is organized along east to west (5% of total lava flows), NE-SW (25% of total lava flows), NW-SE (25% of total lava flows), SE-NW (25%), and SW-NE (20% of total lava flows).
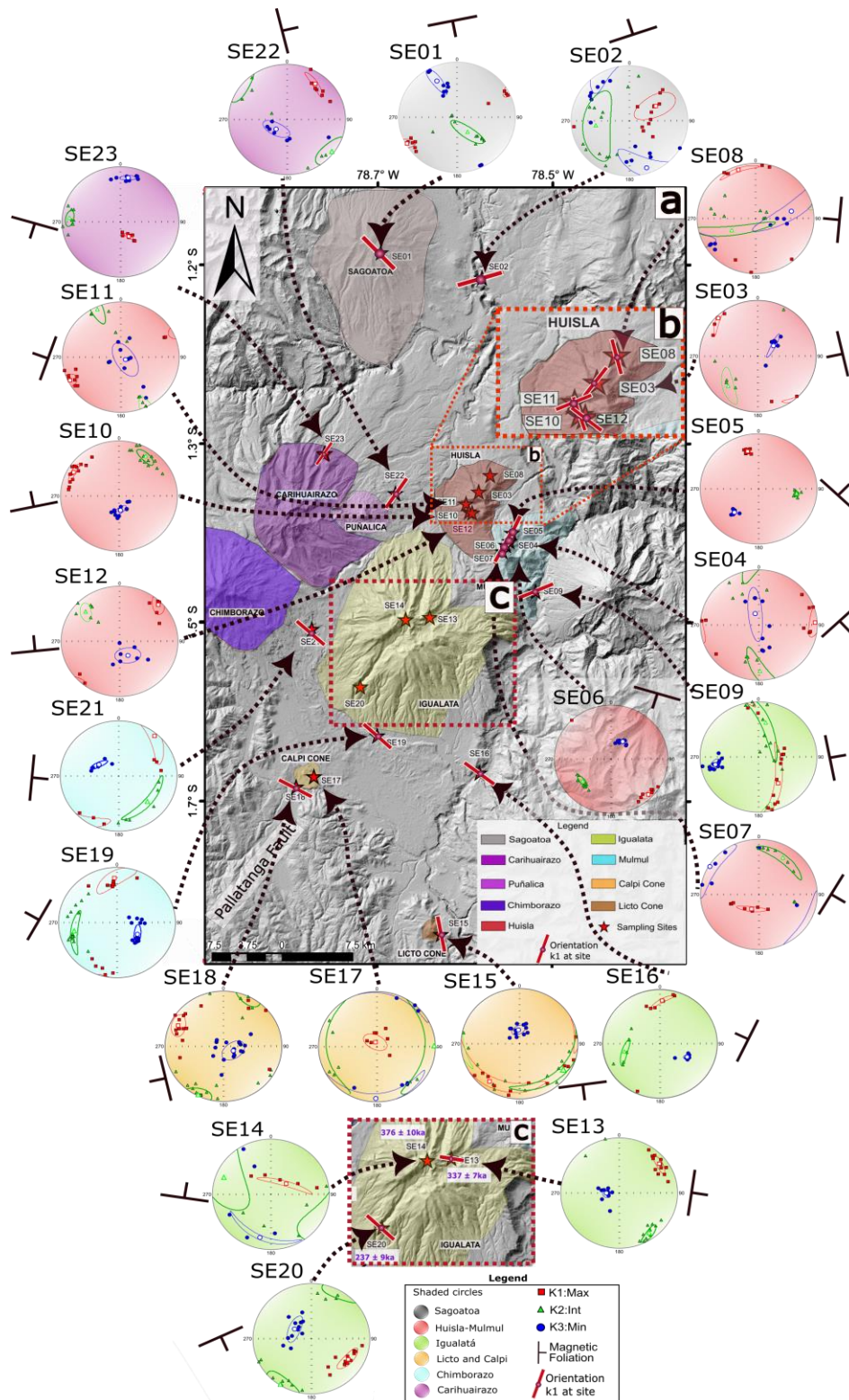
Figure 16. a) Overall AMS directions on a map. The principal susceptibility directions (k1:kmax) are added onto the southern end of the Ecuadorian arc map. The distribution of the magnetic foliations (K₃) is shown. Where a red square is the k1, a green triangle is k2, and the blue circle is k3; b) red pointed square represents a zoom of the Huisla volcano; and c) red pointed square represents a zoom of the Igualatá volcano.

5.3. Paleomagnetism

After 100 mT AF-demagnetization, half of the samples had lost more than 95% of their Natural Remanent Magnetization (NRM) and the rest after 120 mT (Figure 17). Using thermal demagnetization, the samples were completely demagnetized (i.e. more than 98% of NRM lost) between 560 °C and 620 °C (Figure 17; e.g. SE06, SE22). In particular, more than 80% of all samples lost their NRM at around 580 °C. These results indicate that titanomagnetite with poor content of titanium is the main carrier of the magnetization. However, some minor amounts of Ti-hematite could be the cause for stronger resistance to alternating field demagnetization (>100 mT) and unblocking temperatures above 580 °C (Figure 17; e.g., SE02, SE22).

Also, in some cases, the presence of maghemite is observable by the slight inflections at around 350 °C (Figure 17, e.g. SE06). For one site (SE01, Sagoatoa volcano) a secondary direction was not entirely isolated using PCA. In this sample the characteristic direction was obtained by the analysis of converging great circles (Halls, 1976; McFadden & McElhinny, 1988), getting a Maximum Angular Deviation (MAD) below than 5°.
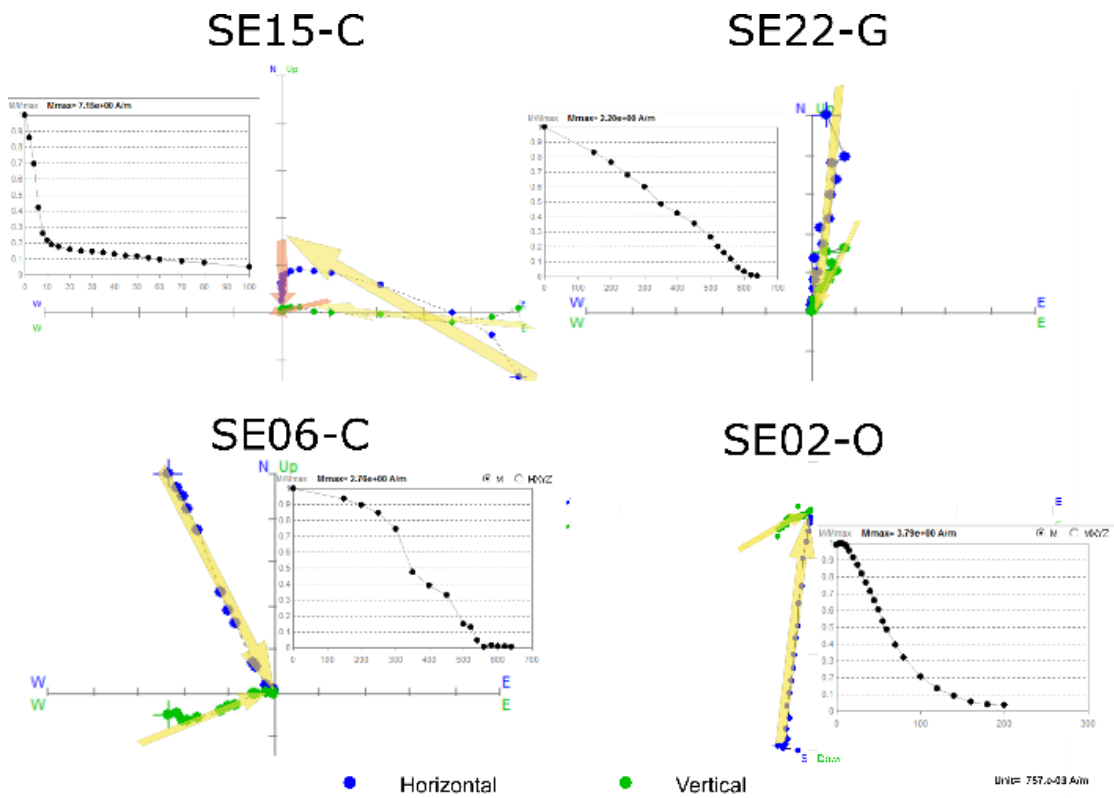
Figure 17. Examples of thermal and alternating field demagnetization diagrams. Zijderveld projections and module plot obtained from SE15, SE22, SE6 and SE2 respectively.

Table 3. Main paleomagnetic directions table. Where: ChRM is characteristic remanent magnetization; Dec is declination; Inc is Inclination; dam: demagnetization analysis method. PCA: principal component analysis, GC: Great Circle; dp: semi-axis of the confidence ellipse along the great circle path from site to pole; and dm: semi-axis of the confidence ellipse perpendicular to that great circle path.

		Site Coordinates			ChRM							Specific Polarity				
Site	Volcano	Latitude°	Longitude°	N/n	Age (ka)	Dec°	Inc°	a95	k	dam	Polarity	Pole long°	Pole lat°	dp	dm	A95
SE03	Huisla-Mulmul	-1.3748	-78.5712	8/8	492 ± 9	331.7	-36.2	4.1	186.6	PCA	N	155.4	56.6	2.8	4.8	4.9
SE4	Huisla-Mulmul	-1.41314	-78.5397	5/8	163 ± 5	350.3	-7	3.9	386.7	PCA	N	179.1	80.1	2	3.9	4.1
SE05	Huisla-Mulmul	-1.42084	-78.5419	8/8	174 ± 3	324.2	-8.2	6.4	75.3	PCA	N	186.4	54.1	3.3	6.5	8.6
SE06	Huisla-Mulmul	-1.42442	-78.5452	8/8	163 ± 3	339.6	10.7	2.5	510	PCA	N	210.1	68.5	1.3	2.5	3.1
SE07	Huisla-Mulmul	-1.43024	-78.5485	5/7	145 ± 4	21.6	49.3	3.5	390.7	PCA	N	312.8	52.3	3	4.6	4.8
SE08	Huisla-Mulmul	-1.35934	-78.5605	7/8	587 ± 9	346.6	13.8	12	42	PCA	N	223.6	74.2	6.3	12.3	15.3
SE09	Igualatá	-1.46754	-78.5171	7/9	371 ± 7	0.9	-2.7	3.8	252.6	PCA	N	4.1	89.1	1.9	3.8	3.9
SE10	Huisla-Mulmul	-1.38589	-78.5833	9/9	612 ± 10	334.7	11.4	6.6	61.12	PCA	N	206.3	61.6	3.4	6.7	9.1
SE11	Huisla-Mulmul	-1.39315	-78.5805	9/9	547 ± 11	350.2	10.5	4.6	125	PCA	N	225.4	78.2	2.3	4.5	5.2
SE12	Huisla-Mulmul	-1.39439	-78.5775	8/8	526 ± 20	12.3	1.5	7.8	51.97	PCA	N	1.6	77.5	3.9	7.8	7
SE13	Igualata	-1.4916	-78.6176	9/9	337 ± 7	9.8	0.6	2.9	311.1	PCA	N	1.1	80	1.5	2.9	3.3

Site	Name	Lat	Long	n/N	Age	D	I	α95	k	Method	Pol					
SE14	Igualatá	-1.49372	-78.6405	6/8	376 ± 10	340.3	-41.4	14.7	22.7	PCA	N	164.3	57.2	10.9	17.9	18.9
SE15	Licto cone	-1.78668	-78.6067	7/8	183 ± 9	1.4	-5.6	4.8	131.9	PCA	N	47.5	88.3	1.9	3.8	3.4
SE16	Igualatá	-1.63636	-78.5701	9/9	358 ± 6	359	23	3	294	PCA	N	277.3	76.3	1.7	3.2	4
SE17	Calpi cone	-1.63993	-78.7275	6/9	16 ± 6	353	-5.3	8.4	63.8	PCA	N	171.5	87.1	4.2	8.5	9.4
SE18	Calpi cone	-1.64961	-78.7446	9/9	62 ± 4	18.6	15.9	3.4	236.6	PCA	N	343.2	69	1.8	3.6	3.8
SE19	Chimborazo	-1.60181	-78.6675	9/9	4 ± 2	351.1	-18.9	2.2	544.2	PCA	N	148.5	78	1.2	2.3	2.9
SE20	Igualatá	-1.55641	-78.6836	9/9	237 ± 9	4.5	-9.9	3.9	176.4	PCA	N	48.8	84.3	2	3.9	5.5
SE21	Chimborazo	-1.50261	-78.7297	7/9	30 ± 3	26.5	14.8	12	42	PCA	N	352.1	62.1	7	13.6	9.9
SE22	Carihuairazo	-1.37637	-78.6504	9/9	18 ± 3	5.1	-12.3	7.3	51.2	PCA	N	55.1	83	3.8	7.4	7.3
SE23	Carihuairazo	-1.33902	-78.7175	6/9	512 ± 9	342.1	-38	8.6	61.2	PCA	N	141.1	63.5	6.1	10.2	9.8
MEAN (21)				159 /179		355.7	-1.7	10.9			N	202.4	85			
SE01	Sagoatoa	-1.15216	-78.6646	5/8	826 ± 12	169.2	1.2	--	--	PCA/ GC	R	194.2	79.2	--	--	--
SE02	Sagoatoa	-1.17572	-78.5683	9/9	799 ± 12	188	12.2	3.1	268.46	PCA	R	43.7	80.6	1.6	3.2	3.1
MEAN (2)				14/17		178.5	6.8	14.3			R	133.5	87.3			

The mean direction for all sites is D = 355.4°, I = -1.1° (A95=7.6°). This result overlaps the prevalent GAD field in the region (D = 0°; I = -2°). However, it is consistent with earlier data published by Opdyke et al. (2006) (D = 359.9°, I = −5.4°, and A95 = 4.2°), which means that this data agrees with a GAD field plus 5% quadrupole (Figure 18). For the Brunhes chron the mean direction is D = 355.7°, I = -1.7° (A95=10.9°) (Figure 18a; Table 1). On the other hand, for the Matuyama chron the mean direction is D = 178.5°, I = 6.8° (A95 = 14.3°) (Figure 18b; Table 2), both directions being consistent with past works on Ecuador (Kent et al., 2010; Opdyke et al., 2006). Finally, the mean paleopole for all samples from Southern Ecuador is: Plat= 85.4° N, and Plong=199.6 E° with an A95=7.6.
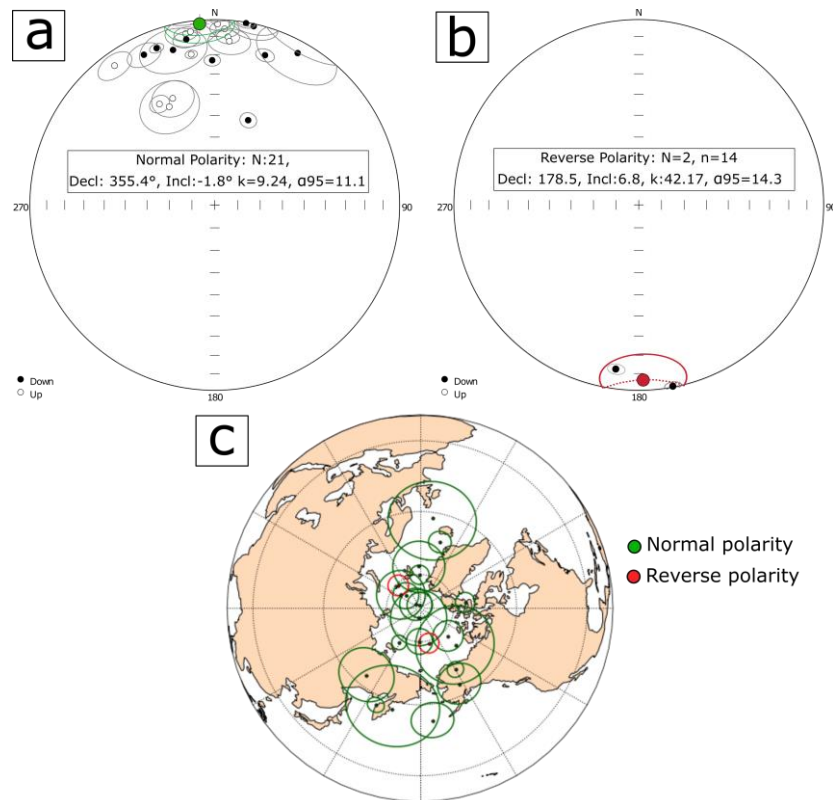
Figure 18. Stereographic projection of (a) normal and (b) reverse polarity for all sampling sites. (c) VGP poles from lava flows belonging to Southern Ecuador. Green and red circles are the errors associates with the poles.

5.3.1. Paleosecular Variation

The VGP dispersion (Sb) as a function of latitude is shown in Figure 19. Taking into account all the data from southern Ecuador, it shows a Sb of 15.6° (Su = 19.10°; Sl = 11.56°, using a Vandamme (1994) cutoff). This result is higher than values predicted by the models G (McFadden et al., 1988) and TK03 (Tauxe & Kent, 2004) (Figure 19). The resulting VGP mean from all sites and combining the Brunhes and Matuyama polarities is located at latitude: 85.1°, longitude: 198.7°, and A95: 7.8° from the 23 VGPs.

Comparing the resulting VGP mean with two past studies in continental and insular Ecuador we found: (1) VGP dispersions obtained previously are lower than our Sb; (2) Opdyke et al. (2006) obtained a Sb of 14.0° (Su = 16.2°; Sl = 12.3°) at 0.6°S in continental Ecuador, (3) Kent et al. (2010) obtained a Sb of 11.4° (Su=13.0°; Sl=10.2°) in insular Ecuador, which is some degrees lower than Opdyke et al. (2006) and this study. The Sb value in Opdyke et al. (2006) is surprisingly close to our estimates, having just a difference of 1.6°. Both values are higher than that expected by G and TK03 models (Figure 19). This higher

dispersion may be related to tectonism, which could rotate or tilt some lava flows due to the continuous formation of the Ecuadorian Andes. Alternatively, but not excluding the previous cause, a higher dispersion can be related to the influence of the South Atlantic Magnetic Anomaly (de Oliveira et al., 2022), which causes strong longitudinal variability of the field associated with important non-dipolar components. As a comparison, Kent et al. (2010) (64 site VGPs; ≈400 samples; from 0 to 3 Ma lavas) obtained a Sb of 11.4° (Su=13.0°; Sl=10.2°) in Galápagos Islands (Ecuador), which is some degrees lower than our estimates.
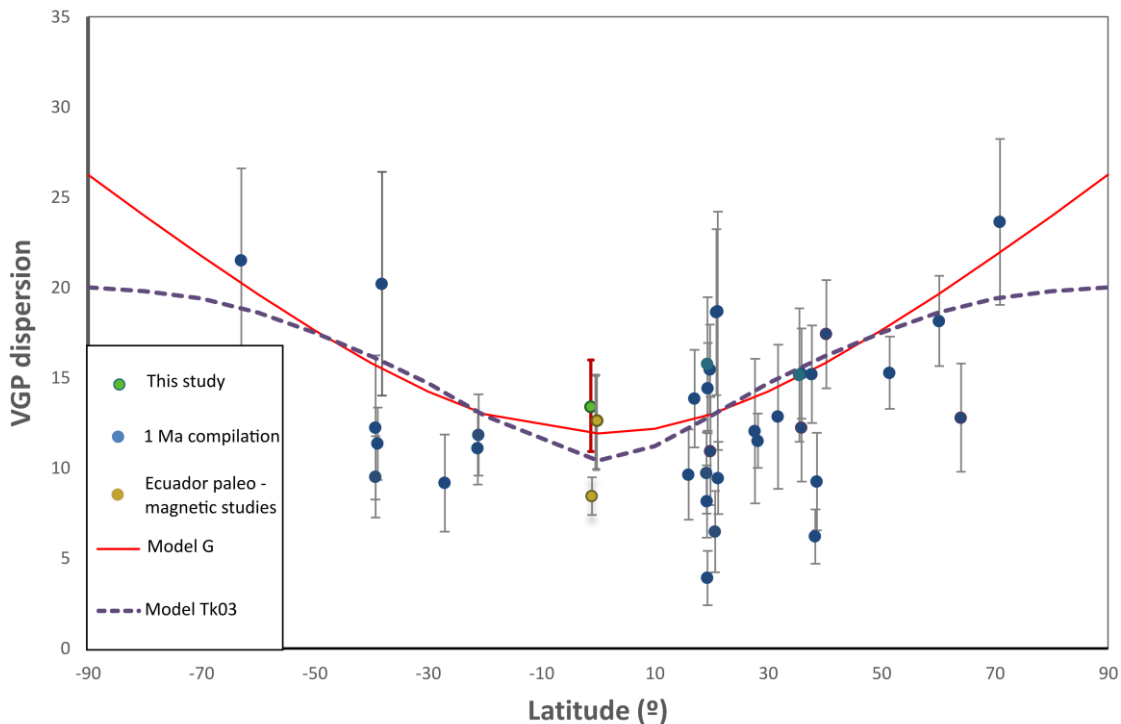
Figure 19. VGP angular dispersion (Sb) versus latitude for southern Ecuador compared to other estimates VGP within the last 1Ma and compared with proposed models (Model G and Model TK03).

5.4. Magnetic Excursions

Two sites have anomalous directions with respect to the GAD assumption at the Equator. One of these two sites fit perfectly in a range of the Orphan Knoll excursion reported by Channell (2017) at ~495 ka. This site correspond to a lava flow dated from 492 ± 9, belonging to Huisla Mulmul volcano (SE03) (Figure 20). Supporting this excursion, Wilson & Hey, (1981) and Thouveny et al. (2008) report a magnetic anomaly at ~0.495 ka in the Galápagos Island (Ecuador) at the time of the Orphan Knoll excursion (Figures 7 and 20). Finally, Ménabréaz et al. (2014) shows a superabundance of Berilium (10) west of the

equatorial Pacific dated at around 495 ka, which is also correlated to the anomalous VGP of SE03 (D= 331.2; I= -37.9; VGP = lat: 55.6°N and long: 154.0°E).

The other site with anomalous directions (SE21) has a K-Ar age of 30 ± 3 ka, which is in the range of the Mono Lake excursion. Hence, based on their similar ages, this is probably a record of the Mono Lake excursion on the Chimborazo lava flow (Figure 20). This excursion was dated between 26 to 32 ka (Liddicoat, 1992; Lund et al., 1988; Negrini et al., 2000), being also supported by low relative paleointensity (RPI) (Liddicoat & Coe, 1979) and by the high concentration of ^{36}Cl (Wagner et al., 2000). A GAD field disturbance could generate peaks of ^{36}Cl, especially when the field is at its minimum. The VGP location of SE21 (lat: 61.2°N and long: 342.8°E) is relatively consistent with the geometry deduced from the VGP path associated with the Mono Lake paleomagnetic excursion (Valet, 2008).
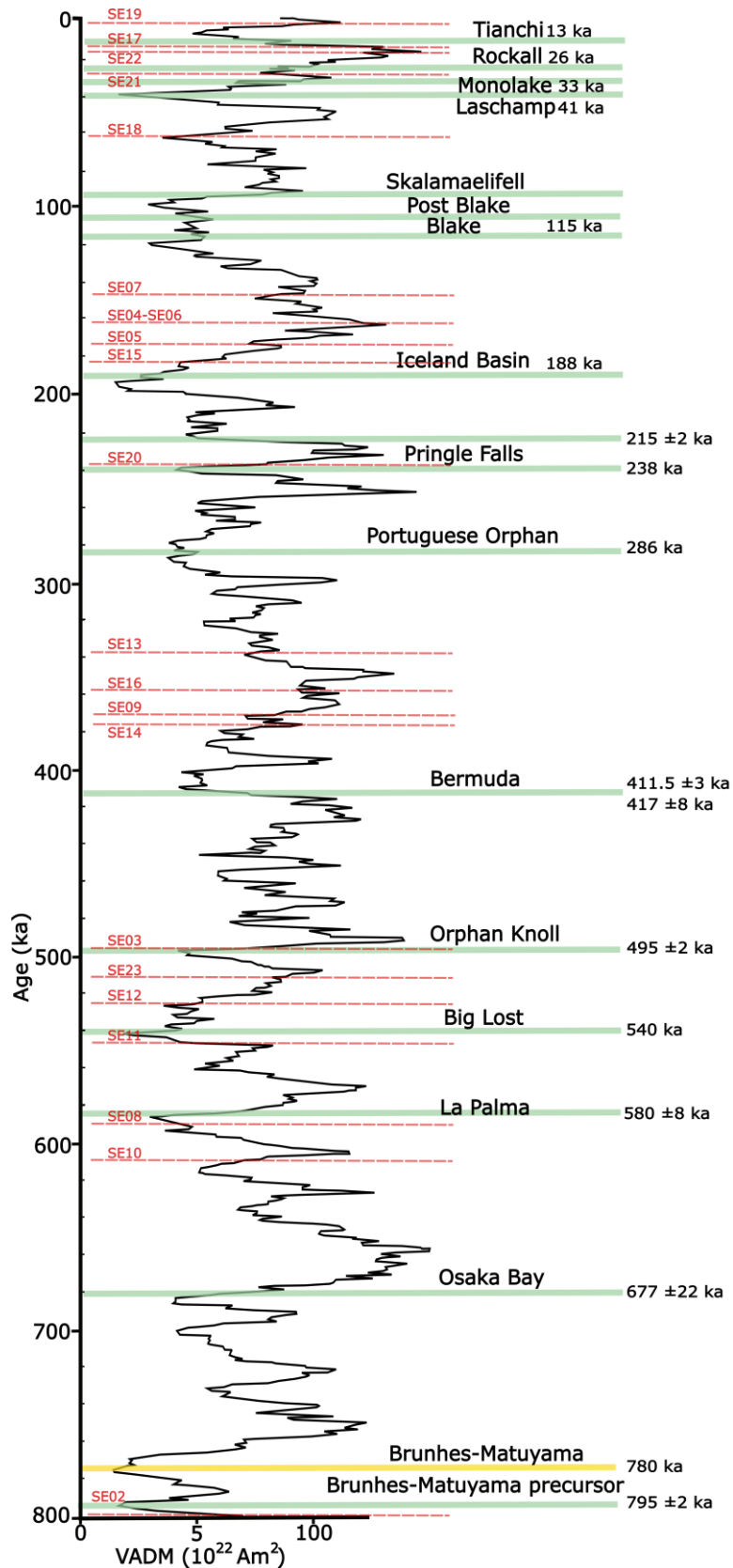
Figure 20. The virtual axial dipole moment (VADM) versus age from the last 0.8 Ma. The main magnetic excursion from the las 1 Ma (Brunhes-Matuyama) is noted as the yellow bar. Red dashed lines represent the age of each side. Green bars represent the diferent magnetic

excursions. Reference excursions are taken from e.g. Channell, (2006); Channell et al., (2009); Negrini et al., (2000); Singer et al., (2019); Thouveny et al., (2008).

5.5. Tectonic Implications

The Pallatanga dextral strike-slip fault segment (Baize et al., 2015; Alvarado et al., 2016) crosses through two volcanoes of this study, the Igualata volcano and the Huisla-Mulmul volcanic complex. This fault started between the Pliocene to Early Pleistocene (Lavenu et al., 1995). Since the formation of Igualata volcano, the Pallatanga fault has produced a valley, with a NE-SW trend that crosses the main volcanic edifice (Baize et al., 2020).

Tectonic deformation features from Igualata volcano (Figure 14b) show that sample SE14 (376 ± 10ka) was affected by this fault, matching the counter slope scarps displacing valley floors and the free-face scarps with an inconsistent VGP (Long: 156.5925675; Lat: 55.11551749). This supports the statement of Baize et al. (2020), which suggest a multiple long term displacement and possible rotation related with the Pallatanga fault in that sector. Furthermore, the SE14 site shows a disturbed magnetic fabric, which could related to either SD titanomagnetites (Potter & Stephenson, 1988) or local deformation changing the lava flow direction indicated by the AMS data (Merle, 1998). Likewise, site SE07 from Huisla Mulmul volcano could have been affected by a fault, but in this case by the Rio Chambo fault (Ordóñez, 2012). This site also shows an inverse magnetic fabric, like site SE14. In sum, the anomalous paleomagnetic directions and AMS data in these two sites (SE14 and SE07) may have been affected by small tilts, rotation or displacemnts related to local tectonics.
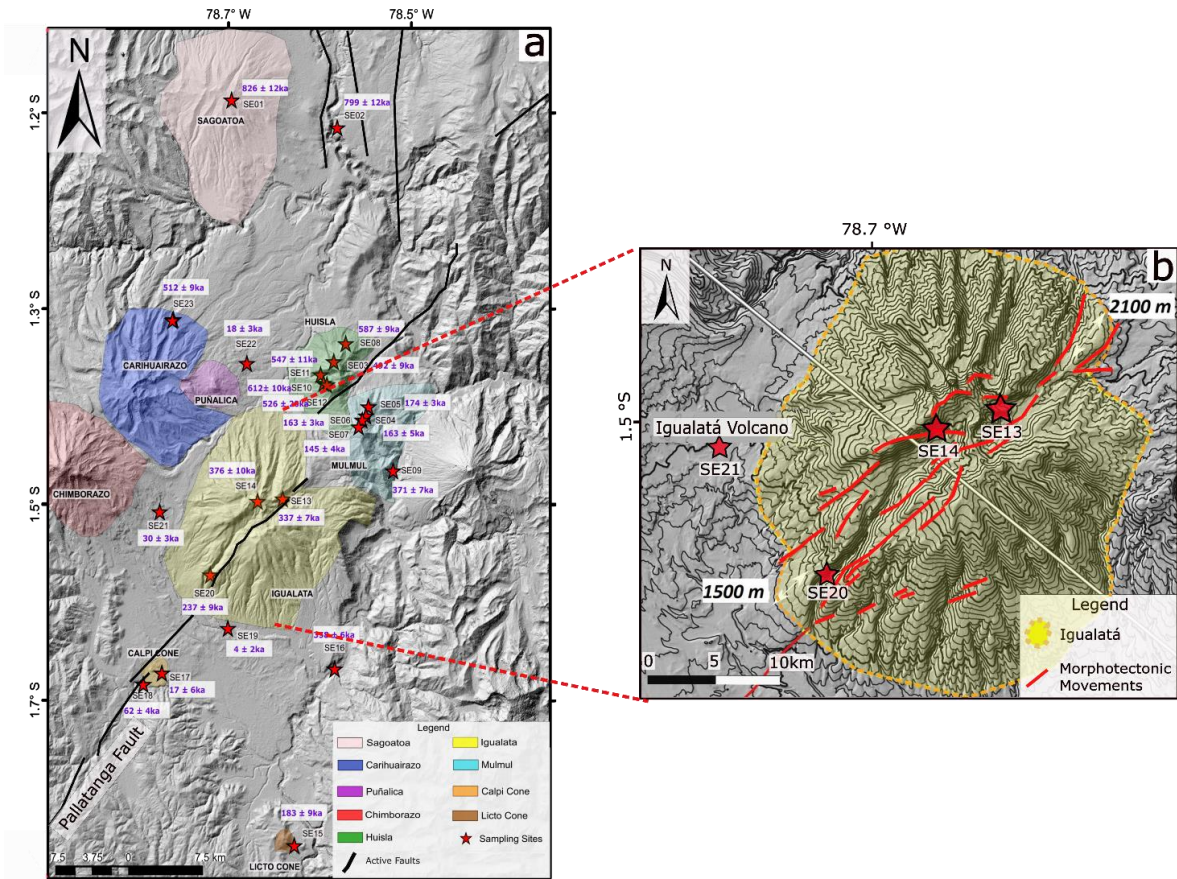
Figure 21. Pallatanga fault segments and morphotectonic movements from Igualatá. a) Study area with the distribution of the different volcanoes and samples sites at the southern end of the Ecuadorian arc. Black lines indicate the location of the Pallatanga fault segments, described in detail in Baize et al. (2016). b) Sagoatoa volcano; DEM picture and related elevation contours (contour spacing: 100 m). Red lines are the morphotectonic lineaments forming the fault zone.

CONCLUSIONS

6. CONCLUSIONS

6.1. AMS, Rock magnetic properties, and tectonism.

A total of 23 well dated (K-Ar) lava flows that covers the last million year belonging to Southern Ecuador were subjected to intensive rock-magnetic analysis. Demagnetization analysis, FORC curves, Day plot, hysteresis and thermomagnetic curves show consistently that the main magnetization carrier is titanomagnetite, being mostly in the PSD state. Specifically, titanium poor titanomagnetites is the main carrier of magnetization from almost all lava flows. Thermomagnetic analysis from Licto and Calpi cones show a special case, in which titanomagnetite rich in titanium is the main carrier of magnetization. Some samples also show the presence of Ti-hematite as a secondary magnetic carrier in the rocks.

Inverse magnetic fabric is noted in four lava flows from different volcanic edifices. It is generally believed that the principal source of inverse fabric may be due to the presence of single domain magnetite. But for our case, those sites are just in the middle of the PSD zone. A syn-magmatic flow fabric is shown for all lava flows (P≤10%). Small tilt, rotation or displacements affect the AMS interpretations, specifically the flow dynamics. A couple of sites (SE04, SE08, and SE14) showed high internal dispersion and could be associated with the viscosity of the lavas and/or lava flow morphology. Specifically, dispersion in SE14 is due to thermal effect from later eruptions. Magnetic foliation from Huisla volcano leads us to interpret this volcano as multiple lava flows fed by a unique crater. Small block rotation could have taken place for two lava flows belong to Mulmul volcano. Furthermore, anomalous paleomagnetic data from these sites, which are titanomagnetite with PSD state and single component, could corroborate the block rotation assumption. The source from all lava flows from Igualatá volcano could possibly have been near SE13 and SE14 and travelled downvalley from there to the east. A lava flow taken on the upper central part of the monogenetic Calpi cone is interpreted as feeder conduit zone. Generally, imbrication and magnetic foliation does not have any consistent regional pattern orientation, even contemporaneous lava flows.

6.2. Rock magnetism and Paleomagnetism

One sample from Huisla Mulmul and one sample from Chimborazo volcano fit perfectly in the path of the Orphan Knoll and Mono Lake paleomagnetic excursions respectively. Our data illustrate that the mean direction (D = 355.4°, I = -1.1° and A95=7.6°) lies inside the error range from past studies on Ecuador. The mean paleopole direction is Plat= 85.4° N, and Plon=199.6 E° with an A_{95}=7.6°. 21 lava flows show a normal polarity and two lava flows lies in the reverse polarity.

Two previous studies showed VGP dispersions lower than our Sb value, being the results from continental Ecuador the closest to our estimates with a difference of 1.6°. Paleosecular variation on continental Ecuador from these previous studies and from our own study is slightly higher than the predicted by G and TK03 models. This contrasts with Galapagos VGP dispersion, which is smaller than both models.

Two sites present anomalous paleomagnetic directions and AMS data, reinforces past tectonic studies that show small tilt, rotation or displacements for Igualata volcano and Huisla-Mulmul volcanic complex. Taken together, morfotectonic movements from Pallatanga fault and an inconsistent VGP from Igualatá volcano (SE14: 376 ± 10ka) suggest tectonic activity has affected these sites.

7. BIBLIOGRAPHY

Atarita, F. R., Bijaksana, S., Ndari, N. R. D. W., Pratama, A., Taqwantara, R. F., Fajar, S. J., & Latief, F. D. E. (2019). Anisotropy of magnetic susceptibility and preferred pore orientation in lava flow from the ijen volcanic complex, East Java, Indonesia. *Geosciences (Switzerland)*, *9*(7). https://doi.org/10.3390/geosciences9070304

Baag, C.-G., & Helsley, C. E. (1974). Geomagnetic secular variation Model E. *Journal of Geophysical Research*, *79*(32), 4918–4922. https://doi.org/10.1029/jb079i032p04918

Bablon, M., Quidelleur, X., Samaniego, P., Le Pennec, J. L., Audin, L., Jomard, H., Baize, S., Liorzou, C., Hidalgo, S., & Alvarado, A. (2019). Interactions between volcanism and geodynamics in the southern termination of the Ecuadorian arc. *Tectonophysics*, *751*, 54–72. https://doi.org/10.1016/j.tecto.2018.12.010

Baize, S., Audin, L., Alvarado, A., Jomard, H., Bablon, M., Champenois, J., Espin, P., Samaniego, P., Quidelleur, X., & Le Pennec, J. L. (2020). Active Tectonics and Earthquake Geology Along the Pallatanga Fault, Central Andes of Ecuador. *Frontiers in Earth Science*, *8*. https://doi.org/10.3389/feart.2020.00193

Balbas, A. M., Koppers, A. A. P., Clark, P. U., Coe, R. S., Reilly, B. T., Stoner, J. S., & Konrad, K. (2018). Millennial-Scale Instability in the Geomagnetic Field Prior to the Matuyama-Brunhes Reversal. *Geochemistry, Geophysics, Geosystems*, *19*(3), 952–967. https://doi.org/10.1002/2017GC007404

Barberi, F., Coltelli, M., Ferrara, G., Innocenti, F., Navarro, J. M., & Santacroce, R. (1988). Plio-Quaternary volcanism in Ecuador. *Geological Magazine*, *125*(1), 1–14. https://doi.org/10.1017/S0016756800009328

Barbetti, M., & Flude, K. (1979). Geomagnetic variation during the late Pleistocene period and changes in the radiocarbon time scale. *Nature*, *279*(5710), 202–205. https://doi.org/10.1038/279202a0

Biggin, A. J., van Hinsbergen, D. J. J., Langereis, C. G., Straathof, G. B., & Deenen, M. H. L. (2008). Geomagnetic secular variation in the Cretaceous Normal Superchron and in the Jurassic. *Physics of the Earth and Planetary Interiors*, *169*(1–4), 3–19. https://doi.org/10.1016/j.pepi.2008.07.004

Bloxham, J. (2000). Sensitivity of the geomagnetic axial dipole to thermal core-mantle interactions. *Nature*, *405*(6782), 63–65. https://doi.org/10.1038/35011045

Bouchez, J. L. (1997). *Granite is Never Isotropic: An Introduction to AMS Studies of Granitic Rocks*. 95–112. https://doi.org/10.1007/978-94-017-1717-5_6

Busse, F. H., & Simitev, R. D. (2008). Toroidal flux oscillation as possible cause of geomagnetic excursions and reversals. *Physics of the Earth and Planetary Interiors*, *168*(3–4), 237–243. https://doi.org/10.1016/j.pepi.2008.06.007

Butler, R. F. (1992). Paleomagnetism: magnetic domains to geologic terranes. *Boston: Blackwell Scientific Publications.*, *319*. https://doi.org/10.5860/choice.29-5708

Cañón-Tapia, E. (2004). Anisotropy of magnetic susceptibility of lava flows and dykes: A historical account. *Geological Society Special Publication*, *238*(1988), 205–225. https://doi.org/10.1144/GSL.SP.2004.238.01.14

Cañón-Tapia, E., Walker, G. P. L., & Herrero-Bervera, E. (1997). The internal structure of lava flows - Insights from AMS measurements II: Hawaiian pahoehoe, toothpaste lava and 'aā'. *Journal of Volcanology and Geothermal Research*, *76*(1–2), 19–46. https://doi.org/10.1016/S0377-0273(96)00073-X

Channell, J. E. T. (2006). Late Brunhes polarity excursions (Mono Lake, Laschamp, Iceland Basin and Pringle Falls) recorded at ODP Site 919 (Irminger Basin). *Earth and Planetary Science Letters*, *244*(1–2), 378–393. https://doi.org/10.1016/j.epsl.2006.01.021

Channell, J. E. T. (2017). Mid-Brunhes magnetic excursions in marine isotope stages 9, 13, 14, and 15 (286, 495, 540, and 590 ka) at N orth A tlantic IODP S ites U1302/3, U1305, and U1306. *Geochemistry Geophysics Geosystems*, *18(2)*, 473–487. https://doi.org/10.1002/2016GC006626.Received

Channell, J. E. T., Hodell, D. A., Singer, B. S., & Xuan, C. (2010). Reconciling astrochronological and 40Ar/39Ar ages for the Matuyama-Brunhes boundary and late Matuyama Chron. *Geochemistry, Geophysics, Geosystems*, *11*(12), 1–21. https://doi.org/10.1029/2010GC003203

Channell, J. E. T., Xuan, C., & Hodell, D. A. (2009). Stacking paleointensity and oxygen isotope data for the last 1.5 Myr (PISO-1500). *Earth and Planetary Science Letters*, *283*(1–4), 14–23. https://doi.org/10.1016/j.epsl.2009.03.012

Collinson, D. W. (1983). Methods in Rock Magnetism and Palaeomagnetism. Techniques and Instrumentat. In *Springer Science & Business Media.*

Constable, C. G., & Parker, R. L. (1988). Statistics of the geomagnetic secular variation for the past 5 m.y. *Journal of Geophysical Research*, *93*(B10). https://doi.org/10.1029/jb093ib10p11569

Cox, A. (1970). Latitude Dependence of the Angular Dispersion of the Geomagnetic Field. *Geophysical Journal of the Royal Astronomical Society*, *20*(3), 253–269. https://doi.org/10.1111/j.1365-246X.1970.tb06069.x

Cox, A. (1975). The frequency of geomagnetic reversals and the symmetry of the nondipole field. *Reviews of Geophysics*, *13*(3), 35–51. https://doi.org/10.1029/RG013i003p00035

Creer, K. M., Irving, E., & Nairn, A. E. M. (1959). Palaeomagnetism of the Great Whin Sill. *Geophysical Journal of the Royal Astronomical Society*, *2*(4), 306–323. https://doi.org/10.1111/j.1365-246X.1959.tb05802.x

Cromwell, G., Johnson, C. L., Tauxe, L., Constable, C. G., & Jarboe, N. A. (2018). PSV10: A Global Data Set for 0–10 Ma Time-Averaged Field and Paleosecular Variation Studies. *Geochemistry, Geophysics, Geosystems*, *19*(5), 1533–1558. https://doi.org/10.1002/2017GC007318

Day, R., Fuller, M., & Schmidt, V. A. (1977). Hysteresis properties of titanomagnetites: Grain-size and compositional dependence. *Physics of the Earth and Planetary Interiors*, *13*(4), 260–267. https://doi.org/10.1016/0031-9201(77)90108-X

de Oliveira, W. P., Hartmann, G. A., Savian, J. F., Nova, G., Parra, M., Biggin, A. J., & Trindade, R. I. F. (2022). Paleosecular variation record from Pleistocene-Holocene lava flows in southern Colombia. *Physics of the Earth and Planetary Interiors*, *332*(August), 106926. https://doi.org/10.1016/j.pepi.2022.106926

Desi Wulan Ndari, N. R., Suryanata, P. B., Bijaksana, S., Dahrin, D., Atarita, F. R., Pratama, A., Hafidz, A., & Fajar, S. J. (2020). Preferred Pore Orientation as a Complement to Anisotropy of Magnetic Susceptibility: A Case Study of Lava Flows From Batur Volcano, Bali, Indonesia. *Frontiers in Earth Science*, *8*(January 2021). https://doi.org/10.3389/feart.2020.578294

Doell, R. R. (1970). Paleomagnetic secular variation study of lavas from the Massif central, France. *Earth and Planetary Science Letters*, *8*(5), 352–362. https://doi.org/10.1016/0012-821X(70)90108-1

Dunlop, D. J. (2002). Theory and application of the Day plot (M rs / M s versus H cr / H c) 2. Application to data for rocks, sediments, and soils . *Journal of Geophysical Research*, *107*(B3), 1–22. https://doi.org/10.1029/2001jb000487

Dunlop, D. J., & Özdemir, Ö. (1997). Rock Magnetism. *Rock Magnetism*, 1–15. https://doi.org/10.1017/cbo9780511612794

Ferré, E. C. (2002). Theoretical models of intermediate and inverse AMS fabrics. *Geophysical Research Letters*, *29*(7), 31-1-31–34. https://doi.org/10.1029/2001GL014367

Fisher, R. (1953). Dispersion on a Sphere. *Proceedings of the Royal Society A: Mathematical, Physical and Engineering Sciences*, *217*(1130), 295–305. https://doi.org/10.1098/rspa.1953.0064

Glatzmaier, G. A., & Roberts, P. H. (1997). Simulating the geodynamo. *Contemporary Physics*, *38*(4), 269–288. https://doi.org/10.1080/001075197182351

Gordon, R. G., & Cox, A. (1980). Calculating palaeomagnetic poles for oceanic plates. *Geophysical Journal of the Royal Astronomical Society*, *63*(3), 619–640. https://doi.org/10.1111/j.1365-246X.1980.tb02642.x

Gubbins, D. (1999). The distinction between geomagnetic excursions and reversals. *Geophysical Journal International*, *137*(1), F1–F4. https://doi.org/10.1046/j.1365-246X.1999.00810.x

Gutscher, M. A., Malavieille, J., Lallemand, S., & Collot, J. Y. (1999). Tectonic segmentation of the North Andean margin: Impact of the Carnegie Ridge collision. *Earth and Planetary Science Letters*, *168*(3–4), 255–270. https://doi.org/10.1016/S0012-821X(99)00060-6

Hall, M. L., & Beate, B. (1991). El Volcanismo Plio-Cuaternario en los Andes del Ecuador. El Paisaje Volcánico de la Sierra Ecuatoriana. *Corp. Edit. Nac., Quito, Pp. 5–18.* https://doi.org/10.1177/0959651819849372

Hall, M. L., Samaniego, P., Le Pennec, J. L., & Johnson, J. B. (2008). Ecuadorian Andes volcanism: A review of Late Pliocene to present activity. *Journal of Volcanology and Geothermal Research*, *176*(1), 1–6. https://doi.org/10.1016/j.jvolgeores.2008.06.012

Hall, M. L., & Wood, C. A. (1985). Volcano-tectonic segmentation of the northern Andes. *Geology*, *13*(3), 203–207. https://doi.org/10.1130/0091-7613(1985)13<203:VSOTNA>2.0.CO;2

Hall, M., & Mothes, P. (2008). The rhyolitic-andesitic eruptive history of Cotopaxi volcano, Ecuador. *Bulletin of Volcanology*, *70*(6), 675–702. https://doi.org/10.1007/s00445-007-0161-2

Halliday, D., Resnick, R., & Bowen, G. H. (1972). Fundamentals of Physics. In *Physics Today* (TENTH EDIT, Vol. 25, Issue 4). John Wiley & Sons, Inc. https://doi.org/10.1063/1.3070817

Halliday, D., Resnick, R., & Bowen, G. H. (2013). Fundamentals of Physics. In *John Wiley & Sons* (Vol. 25, Issue Tenth Edition). https://doi.org/10.1063/1.3070817

Halls, H. C. (1976). A Least-Squares Method to find a Remanence Direction from Converging Remagnetization Circles. *Geophysical Journal of the Royal Astronomical Society*, *45*(2), 297–304. https://doi.org/10.1111/j.1365-246X.1976.tb00327.x

Harrison, C. G. A. (1974). The paleomagnetic record from deep-sea sediment cores. *Earth Science Reviews*, *10*(1), 1–36. https://doi.org/10.1016/0012-8252(74)90024-5

Hartl, P., & Tauxe, L. (1996). A precursor to the Matuyama/Brunhes transition-field instability as recorded in pelagic sediments. *Earth and Planetary Science Letters*, *138*(1–4), 121–135. https://doi.org/10.1016/0012-821x(95)00231-z

Hatakeyama, T., & Kono, M. (2002). Geomagnetic field model for the last 5 My: Time-averaged field and secular variation. *Physics of the Earth and Planetary Interiors*, *133*(1–4), 181–215. https://doi.org/10.1016/S0031-9201(02)00084-5

Hey, R. (1977). Tectonic evolution of the Cocos-Nazca spreading center. *Geol. Soc. Am. Bull., 88(10), 870 1404–1420.* https://doi.org/10.1130/0016-7606(1977)88<i:TEOTCS>2.0.CO;2

Hospers, F. (1954). Reversals of the main geomagnetic field, part III,. *Proc. R. Neth. Acad. Sci., Ser. B, 57, 112–121.*

Hrouda, F., & Schulmann, K. (1990). Conversion of the magnetic susceptibility tensor into the orientation tensor in some rocks. *Physics of the Earth and Planetary Interiors*, *63*(1–2), 71–77. https://doi.org/10.1016/0031-9201(90)90061-2

Hunt, C. P., Moskowitz, B. M., & Banerjee, S. K. (1995). Magnetic Properties of Rocks and Minerals: A Handbook of Physical Constants. *Rock Physics & Phase Relations*, *3*, 189−204.

Irving, E., & Ward, M. A. (1964). A statistical model of the geomagnetic field. *Pure and Applied Geophysics PAGEOPH*, *57*(1), 47–52. https://doi.org/10.1007/BF00879707

Jackson, M., Rochette, P., Fillion, G., Banerjee, S., & Marvin, J. (1993). Rock magnetism of remagnetized Paleozoic carbonates: Low-temperature behavior and susceptibility characteristics. *Journal of Geophysical Research: Solid Earth*, *98*(B4), 6217–6225. https://doi.org/10.1029/92jb01319

Jelinek, V. (1981). Characterization of the magnetic fabric of rocks. *Tectonophysics*, *79*(3–4), 63–67. https://doi.org/10.1016/0040-1951(81)90110-4

Jelínek, V. (1978). Statistical processing of anisotropy of magnetic susceptibility measured on groups of specimens. *Studia Geophysica et Geodaetica*, *22*(1), 50–62. https://doi.org/10.1007/BF01613632

Johnson, C. L., Constable, C. G., Tauxe, L., Barendregt, R., Brown, L. L., Coe, R. S., Layer, P., Mejia, V., Opdyke, N. D., Singer, B. S., Staudigel, H., & Stone, D. B. (2008). Recent investigations of the 0-5 Ma geomagnetic field recorded by lava flows. *Geochemistry, Geophysics, Geosystems*, *9*(4). https://doi.org/10.1029/2007GC001696

Johnson, C. L., & McFadden, P. (2015). The Time-Averaged Field and Paleosecular Variation. In *Treatise on Geophysics: Second Edition* (Vol. 5). Published by Elsevier Inc. https://doi.org/10.1016/B978-0-444-53802-4.00105-6

Johnson, H. P., & Merrill, R. T. (1972). Magnetic and mineralogical changes associated with low-temperature oxidation of magnetite. *Journal of Geophysical Research*, *77*(2), 334–341. https://doi.org/10.1029/jb077i002p00334

Kent, D. V., & Tauxe, L. (2005). Corrected late triassic latitudes for continents adjacent to the North Atlantic. *Science*, *307*(5707), 240–244. https://doi.org/10.1126/science.1105826

Kent, D. V., Wang, H., & Rochette, P. (2010). Equatorial paleosecular variation of the geomagnetic field from 0 to 3 Ma lavas from the Galapagos Islands. *Physics of the Earth and Planetary Interiors*, *183*(3–4), 404–412. https://doi.org/10.1016/j.pepi.2010.08.010

Kirschvink, J. L. (1980). The least-squares line and plane and the analysis of palaeomagnetic data. *Geophysical Journal of the Royal Astronomical Society*, *62*(3), 699–718. https://doi.org/10.1111/j.1365-246X.1980.tb02601.x

Laj, C., & Channell, J. E. T. (2007). Geomagnetic Excursions. *Geomagnetic Excursions. Geomagnetism, 5*, 373–416.

Langereis, C. G., Dekkers, M. J., De Lange, G. J., Paterne, M., & Van Santvoort, P. J. M. (1997).

Magnetostratigraphy and astronomical calibration of the: Last 1.1 Myr from an eastern Mediterranean piston core and dating of short events in the Brunhes. *Geophysical Journal International*, *129*(1), 75–94. https://doi.org/10.1111/j.1365-246X.1997.tb00938.x

Langereis, G., Krijgsman, W., Muttoni, G., & Menning, M. (2010). Magnetostratigraphy-concepts, definitions, and applications. *Newsletters on Stratigraphy*, *43*(3), 207–233. https://doi.org/10.1127/0078-0421/2010/0043-0207

Lavenu, A., Noblet, C., Bonhomme, M. G., Egüez, A., Dugas, F., & Vivier, G. (1992). New KAr age dates of Neogene and Quaternary volcanic rocks from the Ecuadorian Andes: Implications for the relationship between sedimentation, volcanism, and tectonics. *Journal of South American Earth Sciences*, *5*(3–4), 309–320. https://doi.org/10.1016/0895-9811(92)90028-W

Lavenu, A., Winter, T., & Dávila, F. (1995). A Pliocene-Quaternary compressional basin in the Interandean Depression, Central Ecuador. *Geophysical Journal International*, *137*(1), 279–300. https://doi.org/10.1111/j.1365-246X.1995.tb03527.x

Liddicoat, J. C. (1992). Mono Lake excursion in Mono Basin, California, and at Carson Sink and Pyramid Lake, Nevada. *Geophysical Journal International*, *108(2)*, 442–452. https://doi.org/https://doi.org/10.1111/j.1365-246X.1992.tb04627.x

Liddicoat, J. C., & Coe, R. S. (1979). Mono Lake geomagnetic excursion. *Journal of Geophysical Research: Solid Earth*, *84*(B1), 261–271. https://doi.org/10.1029/jb084ib01p00261

Lindsley, D. H. ., Andreasen, G. E., & Balsey, J. R. (1966). Magnetic Properties of Rocks and Minerals. *THE GEOLOGICAL SOCIETY OF AMERICA MEMOIR 97* ,. https://doi.org/doi: 10.1130/MEM97-p543

Lund, S. P., Liddicoat, J. C., Lajoie, K. R., Henyey, T. L., & Robinson, S. W. (1988). Paleomagnetic evidence for long-term (104 year) memory and periodic behavior in the Earth's core dynamo process. *Geophysical Research Letters*, *15*(10), 1101–1104. https://doi.org/https://doi.org/10.1029/GL015i010p01101

Mcelhinny, M. W. (1973). Palaeomagnetism and Plate Tectonics (Cambridge Earth Science Series). *Cambridge University Press*.

McElhinny, M. W., & McFadden, P. L. (1997). Palaeosecular variation over the past 5 Myr based on a new generalized database. *Geophysical Journal International*, *131*(2), 240–252. https://doi.org/10.1111/j.1365-246X.1997.tb01219.x

McElhinny, M. W., & McFadden, P. L. (1999). Paleomagnetism: continents and oceans. *Elsevier*.

Mcelhinny, M. W., McFadden, P. L., & Merrill, R. T. (1996). The time-averaged paleomagnetic field 0-5 Ma. *Journal of Geophysical Research: Solid Earth*, *101(B11)*, 25007–25027. https://doi.org/10.1029/96jb01911

McElhinny, M. W., McFadden, P. L., & Merrill, R. T. (1996). The time-averaged palcomagnetic field 0-5 Ma. *Journal of Geophysical Research: Solid Earth*, *101(B11)*, 25007–25027.

McElhinny, M. W., & Merrill, R. T. (1975). Geomagnetic secular variation over the past 5 m.y. *Reviews of Geophysics*, *13*(5), 687–708. https://doi.org/10.1029/RG013i005p00687

McFadden, P. L., & McElhinny, M. W. (1984). A physical model for palaeosecular variation. *Geophysical Journal of the Royal Astronomical Society*, *78*(3), 809–830. https://doi.org/10.1111/j.1365-246X.1984.tb05072.x

McFadden, P. L., & McElhinny, M. W. (1988). The combined analysis of remagnetization circles and direct observations in palaeomagnetism. *Earth and Planetary Science Letters*, *87*(1–2), 161–172. https://doi.org/10.1016/0012-821X(88)90072-6

Mcfadden, P. L., Merrill, R. T., & Mcelhinny, M. W. (1988). Dipole / Quadrupole Family Modeling of Paleosecular Variation. *Journal of Geophysical Research*, *93*(7).

Mcfadden, P. L., Merrill, R. T., McElhinny, M. W., & LEE, S. (1991). Reversals of the Earth's Magnetic Field and Temporal Variations of the Dynamo Families. *JOURNAL OF GEOPHYSICAL RESEARCH, VOL. 96*, *N*, 3923–3933. https://doi.org/doi:10.1029/90jb02275

Ménabréaz, L., Thouveny, N., Bourlès, D. L., & Vidal, L. (2014). The geomagnetic dipole moment variation between 250 and 800 ka BP reconstructed from the authigenic 10Be/9Be signature in West Equatorial Pacific sediments. *Earth and Planetary Science Letters*, *385*, 190–205. https://doi.org/10.1016/j.epsl.2013.10.037

Merle, O. (1998). Internal strain within lava flows from analogue modelling. *Journal of Volcanology and Geothermal Research*, *81*(3–4), 189–206. https://doi.org/10.1016/S0377-0273(98)00009-2

Merrill, R. T., & McElhinny, M. W. (1983). The Earth's Magnetic Field: Its History, Origin and Planetary Perspective. *International Geophysics*, *32*. https://doi.org/10.1016/S0074-6142(08)60394-0

Merrill, R. T., McElhinny, W., & L.McFadden, P. (1998). The magnetic field of the Earth: paleomagnetism, the core, and the deep mantle (Vol. 63). *International Geophysics Series (Academic Press)*.

Merrill, R. T., & McFadden, P. L. (2003). The geomagnetic axial dipole field assumption. *Physics of the Earth and Planetary Interiors*, *139*(3–4), 171–185. https://doi.org/10.1016/j.pepi.2003.07.016

Negrini, R. M., Erbes, D. B., Faber, K., Herrera, A. M., Roberts, A. P., Cohen, A. S., Wigand, P. E., & Foit, F. F. (2000). A paleoclimate record for the past 250,000 years from Summer Lake, Oregon, USA: I. Chronology and magnetic proxies for lake level. *Journal of Paleolimnology*, *24*(2), 125–149. https://doi.org/10.1023/A:1008144025492

Opdyke, N. D., Hall, M., Mejia, V., Huang, K., & Foster, D. A. (2006). Time-averaged field at the equator:

Results from Ecuador. *Geochemistry, Geophysics, Geosystems*, *7*(11), 1–16. https://doi.org/10.1029/2005GC001221

Opdyke, N. D., & Henry, K. W. (1969). A test of the dipole hypothesis. *Earth and Planetary Science Letters*, *6*(2), 139–151. https://doi.org/10.1016/0012-821X(69)90132-0

Ordóñez, J. (2012). *Depósitos volcánicos del Pleistoceno Tardío en la cuenca de Ambato: caracterización, distribución y origen*. 213. http://bibdigital.epn.edu.ec/handle/15000/4868

Pike, C. R., Roberts, A. P., Dekkers, M. J., & Verosub, K. L. (2001). An investigation of multi-domain hysteresis mechanisms using FORC diagrams. *Physics of the Earth and Planetary Interiors*, *126*(1–2), 11–25. https://doi.org/10.1016/S0031-9201(01)00241-2

Pike, C. R., Roberts, A. P., & Verosub, K. L. (1999). Characterizing interactions in fine magnetic particle systems using first order reversal curves. *Journal of Applied Physics*, *85*(9), 6660–6667. https://doi.org/10.1063/1.370176

Potter, D. K., & Stephenson, A. (1988). *Single-domain particles in rocks and magnetic fabric analysis*. *15*(10), 1097–1100. https://doi.org/https://doi.org/10.1029/GL015i010p01097

Quidelleur, X., & Courtillot, V. (1996). On low-degree spherical harmonic models of paleosecular variation. *Physics of the Earth and Planetary Interiors*, *95*(1–2), 55–77. https://doi.org/10.1016/0031-9201(95)03115-4

Roberts, A. P. (2008). Geomagnetic excursions: Knowns and unknowns. *Geophysical Research Letters*, *35*(17), 1–7. https://doi.org/10.1029/2008GL034719

Roberts, A. P., Pike, C. R., & Verosub, K. L. (2000). First-order reversal curve diagrams: A new tool for characterizing the magnetic properties of natural samples. *Journal of Geophysical Research: Solid Earth*, *105*(B12), 28461–28475. https://doi.org/10.1029/2000jb900326

Rochette, P., Jackson, M., & Aubourg, C. (1992). Rock magnetism andn the interpretation of magnetic susceptibility. *Reviews of Geophysics*, *30*(3), 209–226.

Roperch, P., Chauvin, A., Lara, L. E., & Moreno, H. (2015). Secular variation of the Earth's magnetic field and application to paleomagnetic dating of historical lava flows in Chile. *Physics of the Earth and Planetary Interiors*, *242*, 65–78. https://doi.org/10.1016/j.pepi.2015.03.005

Sagnotti, L. (2007). Iron Sulfides. In *Encyclopedia of Geomagnetism and Paleomagnetism* (pp. 454–459.). https://doi.org/doi:10.1007/978-1-4020-4423-6_160

Samaniego, P., Barba, D., Robin, C., Fornari, M., & Bernard, B. (2012). Eruptive history of Chimborazo volcano (Ecuador): A large, ice-capped and hazardous compound volcano in the Northern Andes. *Journal of Volcanology and Geothermal Research*, *221–222*, 33–51.

https://doi.org/10.1016/j.jvolgeores.2012.01.014

Samaniego, P., Monzier, M., Robin, C., & Hall, M. L. (1998). Late Holocene eruptive activity at Nevado Cayambe volcano, Ecuador. *Bulletin of Volcanology*, *59*(7), 451–459. https://doi.org/10.1007/s004450050203

Schöbel, S., & de Wall, H. (2014). AMS–NRM interferences in the Deccan basalts: Toward an improved understanding of magnetic fabrics in flood basalts. *Journal of Geophysical Research, Solid Eart*(119(4)), 2651–2678. https://doi.org/https://doi.org/10.1002/2013JB010660

Singer, B. S., Hoffman, K. A., Schnepp, E., & Guillou, H. (2008). Multiple Brunhes Chron excursions recorded in the West Eifel (Germany) volcanics: Support for long-held mantle control over the non-axial dipole field. *Physics of the Earth and Planetary Interiors*, *169*(1–4), 28–40. https://doi.org/10.1016/j.pepi.2008.05.001

Singer, B. S., Jicha, B. R., Mochizuki, N., & Coe, R. S. (2019). Synchronizing volcanic, sedimentary, and ice core records of Earth's last magnetic polarity reversal. *Science Advances*, *5*(8), 1–12. https://doi.org/10.1126/sciadv.aaw4621

Spikings, R. A., Winkler, W., Seward, D., & Handler, R. (2001). Along-strike variations in the thermal and tectonic response of the continental Ecuadorian Andes to the collision with heterogeneous oceanic crust. *Earth and Planetary Science Letters*, *186*(1), 57–73. https://doi.org/10.1016/S0012-821X(01)00225-4

Tauxe, L., Banerjee, S. K., Butler, R. F., & Van der Voo, R. (2010). Essentials of Paleomagnetism. *Univ of California Press.*

Tauxe, L., Constable, C., Johnson, C. L., Koppers, A. A. P., Miller, W. R., & Staudigel, H. (2003). Paleomagnetism of the southwestern U.S.A. recorded by 0-5 Ma igneous rocks. *Geochemistry, Geophysics, Geosystems*, *4*(4). https://doi.org/10.1029/2002GC000343

Tauxe, L., & Kent, D. V. (2004). A simplified statistical model for the geomagnetic field and the detection of shallow bias in paleomagnetic inclinations: Was the ancient magnetic field dipolar? *Geophysical Monograph Series*, *145*, 101–115. https://doi.org/10.1029/145GM08

Tauxe, L., & Kodama, K. P. (2009). Paleosecular variation models for ancient times: Clues from Keweenawan lava flows. *Physics of the Earth and Planetary Interiors*, *177*(1–2), 31–45. https://doi.org/10.1016/j.pepi.2009.07.006

Tauxe, L., Mullender, T. A. T., & Pick, T. (1996). Potbellies, wasp-waists, and superparamagnetism in magnetic hysteresis. *Journal of Geophysical Research: Solid Earth*, *101*(1), 571–583. https://doi.org/10.1029/95jb03041

Thouveny, N., Bourlès, D. L., Saracco, G., Carcaillet, J. T., & Bassinot, F. (2008). Paleoclimatic context of geomagnetic dipole lows and excursions in the Brunhes, clue for an orbital influence on the geodynamo?

Earth and Planetary Science Letters, *275*(3–4), 269–284. https://doi.org/10.1016/j.epsl.2008.08.020

Veikkolainen, T., Pesonen, L., & Korhonen, K. (2014). An analysis of geomagnetic field reversals supports the validity of the Geocentric Axial Dipole (GAD) hypothesis in the Precambrian. *Precambrian Research*, *244*(1), 33–41. https://doi.org/10.1016/j.precamres.2013.10.009

Verwey, E. . (1939). Electronic conduction of Magnetite(Fe3O4) and its transition point at low temperature. *Nature*, *144*, 327–328.

Wagner, G., Beer, J., Laj, C., Kissel, C., Masarik, J., Muscheler, R., & Synal, H. A. (2000). Chlorine-36 evidence for the Mono Lake event in the summit GRIP ice core. *Earth and Planetary Science Letters*, *181*(1–2), 1–6. https://doi.org/10.1016/S0012-821X(00)00196-5

Wasilewski, P. J. (1973). Magnetic hysteresis in natural materials. *Earth and Planetary Science Letters*, *20*(1), 67–72. https://doi.org/10.1016/0012-821X(73)90140-4

Wilson, D. S., & Hey, R. N. (1981). THE GALAPAGOS AXIAL MAGNETIC ANOMALY: EVIDENCE FOR THE EMPEROR EVENT WITHIN THE BRUNI{ES AND FOR A TWO-LAYER MAGNETIC SOURCE. *Geophysical Research Letters*, *8*(10), 1051–1054. https://doi.org/https://doi.org/10.1029/GL008i010p01051

Wilson, R. L. (1970). Permanent Aspects of the Earth's Non-dipole Magnetic Field over Upper Tertiary Times. *Geophysical Journal of the Royal Astronomical Society*, *19*(4), 417–437. https://doi.org/10.1111/j.1365-246X.1970.tb06056.x

Wilson, R. L. (1971). Dipole Offset–The Time-Average Palaeomagnetic Field Over the Past 25 Million Years. *Geophysical Journal of the Royal Astronomical Society*, *22*(5), 491–504. https://doi.org/10.1111/j.1365-246X.1971.tb03616.x

Witt, C., Bourgois, J., Michaud, F., Ordoñez, M., Jiménez, N., & Sosson, M. (2006). Development of the Gulf of Guayaquil (Ecuador) during the Quaternary as an effect of the North Andean block tectonic escape. *Tectonics*, *25*(3), 1–22. https://doi.org/10.1029/2004TC001723

Appendix 1

Supplementary table 1. A day plot from all volcanoes in this study. Where Ms: saturation magnetization; Mrs: remanent saturation magnetization; Hc: coercivity; Hcr: coercivity of remanence.

Age	Notes	Data	Volcano	ID	Hc	Mr	Ms	Hcr	Hcr/Hc	Mr/Ms
826 ± 12	R	2021	Sagoatoa 16EQ40	SE01	7.06	74.95	1324	36.73	5.20	0.0566
799 ± 12	R	2021	Sagoatoa 16EQ03	SE02	16.67	174.7	1198.3	39.28	2.36	0.1458
492 ± 9	N	2021	Huisla-Mulmul RIO-111	SE03	28.91	123.74	468.4	58.49	2.02	0.2642
163 ± 5	N	2021	Huisla-Mulmul 16EQ09	SE04	10.35	196.13	1643.7	43.56	4.21	0.1193
174 ± 3	N	2021	Huisla-Mulmul 16EQ08	SE05	8.43	148.41	1595	28.7	3.40	0.0930
163 ± 3	N	2021	Huisla-Mulmul 16EQ10	SE06	10.68	147.48	1295	29.96	2.81	0.1139
145 ± 4	N	2021	Huisla-Mulmul 16EQ11	SE07	13.59	196.96	1338.8	30.64	2.25	0.1471
587 ± 9	N	2021	Huisla-Mulmul 16EQ04	SE08	9.78	234.79	1946.2	32.95	3.37	0.1206
371 ± 7	N	2021	Huisla-Mulmul 16EQ07	SE10	12.99	166.32	1299	31.76	2.44	0.1280
612 ± 10	N	2021	Huisla-Mulmul RIO-107	SE11	5.72	126.92	1352	16.2	2.83	0.0939
547 ± 11	N	2021	Huisla-Mulmul 16EQ05	SE12	8.61	198.35	2014.6	25.77	2.99	0.0985
526 ± 20	N	2021	Igualata 16EQ14	SE09	11.29	100.14	1080	35.93	3.18	0.0927
337 ± 7	N	2021	Igualata 16EQ24	SE13	11.34	133.28	1260	34.67	3.06	0.1058
376 ± 10	N	2021	Igualata 16EQ23	SE14	11.76	160.82	859.89	23.06	1.96	0.1870
183 ± 9	N	2021	Igualata 16EQ29	SE20	15.85	185	820.25	30	1.89	0.2250
358 ± 6	N	2021	Igualata 16EQ27	SE16	10.9	156.4	1591.9	32.44	2.98	0.0982
16 ± 6	N	2021	Licto cone 16EQ47	SE15	7	102.78	923.02	20.6	2.94	0.1114
62 ± 4	N	2021	Calpi 16EQ34	SE17	18.11	227.29	1327.4	38.57	2.13	0.1712
4 ± 2	N	2021	Calpi 17EQ114	SE18	9	143.61	1169.3	36.07	3.82	0.1228
237 ± 9	N	2021	Chimborazo 16EQ28	SE19	8.2	112.11	1115.3	71.3	8.70	0.1005
30 ± 3	N	2021	Chimborazo 16EQ43	SE21	7.8	83.08	677.76	38.61	4.95	0.1226
18 ± 3	N	2021	Carihuairazo RIO-18	SE22	10.38	117.28	852.63	26.27	2.53	0.1376
512 ± 9	N	2021	Carihuairazo CAR-14	SE23-C	10.12	145.13	1635.4	30.49	3.01	0.0887
512 ± 9	N	2021	Carihuairazo CAR-14	SE23-L	6.66	117.27	1544.5	24.21	3.64	0.0759

sd	
psd	
md	
sp	